FERMILAB-PUB-11-394-AE-CD

The serendipitous observation of a gravitationally lensed galaxy at z = 0.9057 from the Blanco Cosmology Survey: The Elliot Arc

E. J. Buckley-Geer,[1] H. Lin,[1] E. R. Drabek, [1,19] S. S. Allam,[1] D. L. Tucker,[1] R. Armstrong,[2] W. A. Barkhouse,[3] E. Bertin,[4] M. Brodwin, [5,6] S. Desai,[15] J. A. Frieman,[1,7] S. M. Hansen,[8] F. W. High,[7] J. J. Mohr,[9,10,11] Y.-T. Lin,[12,13] C.-C. Ngeow,[14,15] A. Rest,[16] R. C. Smith,[17] J. Song,[18] A. Zenteno,[9,10]

ABSTRACT

[1]Center for Particle Astrophysics, Fermi National Accelerator Laboratory, P.O. Box 500, Batavia, IL 60510

[2]National Center for Supercomputing Applications,University of Illinois, 1205 West Clark Street, Urbanan, IL 61801

[3]Department of Physics & Astrophysics,University of North Dakota, Grand Forks, ND 58202

[4]Institut d'Astrophysique de Paris, UMR 7095 CNRS, Université Pierre et Marie Curie, 98 bis boulevard Arago, F-75014 Paris, France

[5]Harvard-Smithsonian Center for Astrophysics, 60 Garden Street, Cambridge, MA 02138

[6]W. M. Keck Postdoctoral Fellow at the Harvard-Smithsonian Center for Astrophysics

[7]University of Chicago, 5640 South Ellis Avenue, Chicago, IL 60637

[8]National Science Foundation Astronomy & Astrophysics Postdoctoral Fellow, University of California Observatories & Department of Astronomy, University of California, Santa Cruz, CA 95064

[9]Department of Physics, Ludwig-Maximilians-Universität, Scheinerstr. 1, 81679 München, Germany

[10]Excellence Cluster Universe, Boltzmannstr. 2, 85748 Garching, Germany

[11]Max-Planck-Institut für extraterrestrische Physik, Giessenbachstr. 85748 Garching, Germany

[12]Institute for Physics and Mathematics of the Universe, University of Tokyo, 5-1-5 Kashiwa-no-ha, Kashiwa-shi, Chiba 277- 8568, Japan

[13]Institute of Astronomy & Astrophysics, Academia Sinica, Taipei, Taiwan

[14]Graduate Institute of Astronomy, National Central University, No. 300 Jonghda Rd, Jhongli City 32001 Taiwan

[15]Department of Astronomy, University of Illinois, 1002 West Green Street, Urbana, IL 61801

[16]Space Telescope Science Institute, 3700 San Martin Dr., Baltimore, MD 21218

[17]Cerro Tololo Inter-American Observatory, National Optical Astronomy Observatory, La Serena, Chile

[18]Department of Physics, University of Michigan, 450 Church St. Ann Arbor, MI 48109

[19]School of Physics, University of Exeter, Stocker Road, Exeter EX4 4QL, United Kingdom

We report on the serendipitous discovery in the Blanco Cosmology Survey (BCS) imaging data of a $z = 0.9057$ galaxy that is being strongly lensed by a massive galaxy cluster at a redshift of $z = 0.3838$. The lens (BCS J2352-5452) was discovered while examining i- and z-band images being acquired in October 2006 during a BCS observing run. Follow-up spectroscopic observations with the GMOS instrument on the Gemini South 8m telescope confirmed the lensing nature of this system. Using weak plus strong lensing, velocity dispersion, cluster richness N_{200}, and fitting to an NFW cluster mass density profile, we have made three independent estimates of the mass M_{200} which are all very consistent with each other. The combination of the results from the three methods gives $M_{200} = (5.1 \pm 1.3) \times 10^{14} M_{\odot}$, which is fully consistent with the individual measurements. The final NFW concentration c_{200} from the combined fit is $c_{200} = 5.4^{+1.4}_{-1.1}$. We have compared our measurements of M_{200} and c_{200} with predictions for (a) clusters from ΛCDM simulations, (b) lensing selected clusters from simulations, and (c) a real sample of cluster lenses. We find that we are most compatible with the predictions for ΛCDM simulations for lensing clusters, and we see no evidence based on this one system for an increased concentration compared to ΛCDM. Finally, using the flux measured from the [OII]3727 line we have determined the star formation rate (SFR) of the source galaxy and find it to be rather modest given the assumed lens magnification.

Subject headings: gravitational lensing: strong — gravitational lensing: weak — galaxies: high-redshift

1. Introduction

Strong gravitational lenses offer unique opportunities to study cosmology, dark matter, galactic structure, and galaxy evolution. They also provide a sample of galaxies, namely the lenses themselves, that are selected based on total mass rather than luminosity or surface brightness. The majority of lenses discovered in the past decade were found through dedicated surveys using a variety of techniques. For example, the Sloan Digital Sky Survey (SDSS) data have been used to effectively select lens candidates from rich clusters (Hennawi et al. 2008) through intermediate scale clusters (Allam et al. 2007; Lin et al. 2009) to individual galaxies (Bolton et al. 2008; Willis et al. 2006). Other searches using the CFHTLS (Cabanac et al. 2007) and COSMOS fields (Faure et al. 2008; Jackson et al. 2008) have yielded 40 and 70 lens candidates respectively. These searches cover the range of giant arcs with Einstein radii $\theta_{EIN} > 10''$ all the way to small arcs produced by single lens galaxies with $\theta_{EIN} < 3''$.

In this paper we report on the serendipitous discovery of a strongly lensed $z = 0.9057$ galaxy in the Blanco Cosmology Survey (BCS) imaging data. The lens is a rich cluster containing a prominent central brightest cluster galaxy (BCG) and has a redshift of $z = 0.3838$. Cluster-scale lenses are particularly useful as they allow us to study the effects of strong lensing in the core of the cluster and weak lensing in the outer regions. Strong lensing provides constraints on the mass contained within the Einstein radius of the arcs whereas weak lensing provides information on the mass profiles in the outer reaches of the cluster. Combining the two measurements allows us to make tighter constraints on the mass M_{200} and the concentration c_{200}, of an NFW (Navarro, Frenk, & White 1995) model of the cluster mass density profile, over a wider range of radii than would be possible with either method alone (Natarajan et al. 1998, 2002; Bradač et al. 2006, 2008a,b; Diego et al. 2007; Limousin et al. 2007; Hicks et al. 2007; Deb et al. 2008; Merten et al. 2009; Oguri et al. 2009). In addition, if one has spectroscopic redshifts for the member galaxies one can determine the cluster velocity dispersion, assuming the cluster is virialized, and hence obtain an independent estimate for M_{200} (Becker et al. 2007). Finally one can also derive an M_{200} estimate from the maxBCG cluster richness N_{200} (Hansen et al. 2005; Johnston et al. 2007). These three different methods, strong plus weak lensing, cluster velocity dispersion, and optical richness, provide independent estimates of M_{200} (M_{200} is defined as the mass within a sphere of overdensity 200 times the critical density at the redshift z) and can then be combined to obtain improved constraints on M_{200} and c_{200}. Measurements of the concentration from strong lensing clusters is of particular interest as recent publications suggest that they may be more concentrated than one would expect from ΛCDM models (Broadhurst & Barkana 2008; Oguri & Blandford 2009).

The paper is organized as follows. In § 2 we describe the Blanco Cosmology Survey. Then in § 3 we discuss the initial discovery and the spectroscopic follow-up that led to confirmation of the system as a gravitational lens, the data reduction, the properties of the cluster, the extraction of the redshifts, and finally the measurement of the cluster velocity dispersion and estimate of the cluster mass. In § 4 we summarize the strong lensing features of the system. In § 5 we describe the weak lensing measurements. In § 6 we present the results of combining of the strong and weak lensing results and the final mass constraints derived from combining the lensing results with the velocity dispersion and richness measurements. We describe the source galaxy star formation rate measurements in § 7 and finally in § 8 we conclude. We assume a flat cosmology with $\Omega_{\rm M} = 0.3$, $\Omega_\Lambda = 0.7$, and $H_0 = 70$ km s^{-1} Mpc^{-1}, unless otherwise noted.

2. The BCS Survey

The Blanco Cosmology Survey (BCS) is a 60-night NOAO imaging survey program (2005-2008), using the Mosaic-II camera on the Blanco 4m telescope at CTIO, that has uniformly imaged 75 $\deg^2$ of the sky in the SDSS *griz* bands in preparation for cluster finding with the South Pole Telescope (SPT) (Vanderlinde et al. 2010) and other millimeter-wave experiments. The depths in each band were chosen to allow the estimation of photometric redshifts for $L \geq L_*$ galaxies out to a redshift of $z = 1$ and to detect galaxies to $0.5L_*$ at 5σ to these same redshifts. The survey was divided into two fields to allow efficient use of the allotted nights between October and December. Both fields lie near $\delta = -55°$ which allows for overlap with the SPT. One field is centered near $\alpha = 23.5$ hr and the other is at $\alpha = 5.5$ hr. In addition to the large science fields, BCS also covers 7 small fields that overlap large spectroscopic surveys so that photometric redshifts (photo-z's) using BCS data can be trained and tested using a sample of over 5,000 galaxies.

3. Discovery of the lens and spectroscopic follow-up

The lens BCS J2351-5452 was discovered serendipitously while examining i- and z-band images being acquired in October 2006 during the yearly BCS observing run. The discoverer (EJB-G) decided to name it "The Elliot Arc" in honor of her then 8 year old nephew. Table 1 lists the observed images along with seeing conditions. Fig. 1 shows a *gri* color image of the source, lens and surrounding environment (the pixel scale is $0.268''$ per pixel). The source forms a purple ring-like structure of radius $\sim 7.5''$ with multiple distinct bright regions. The lens is the BCG at the center of a large galaxy cluster. Photometric measurements estimated the redshift of the cluster at $z \sim 0.4$, using the expected $g - r$ and $r - i$ red sequence colors, and also provided a photo-z for the source of $z \sim 0.7$, as described below.

We obtained Gemini Multi-Object Spectrograph (GMOS) spectra of the source and a number of the neighboring galaxies (Lin et al. 2007). We targeted the regions of the source labeled A1-A4 in Fig. 2, and photometric properties of these bright knots are summarized in Table 2. In addition we selected 51 more objects for a total of 55 spectra. The additional objects were selected using their colors in order to pick out likely cluster member galaxies. Fig. 3 shows the $r - i$ versus i color-magnitude diagram (top plot) and the $g - r$ vs. $r - i$ color-color diagram (bottom plot) of the field. The blue squares in the bottom panel of Fig. 3 show the four targeted knots in the lensed arcs. The green curve is an Scd galaxy model (Coleman, Wu, & Weedman 1980) with the green circles indicating a photometric redshift for the arc of $z \sim 0.7$. Note this is not a detailed photo-z fit, but is just a rough estimate meant to show that the arc is likely at a redshift higher than the cluster redshift. Highest target priority was given to the arc knots and to the BCG. Then cluster red sequence galaxy targets were selected using the simple color cuts $1.55 \leq g - r \leq 1.9$ and $0.6 \leq r - i \leq 0.73$ (also shown in the bottom panel of Fig. 3), which approximate the more detailed final cluster membership criteria described below in §3.2. Red sequence galaxies with $i < 21.6$ ($3''$-diameter SExtractor aperture magnitudes) were selected, with higher priority given to brighter galaxies with $i(3'') \leq 21$. Additional non-cluster targets lying outside the cluster color selection box were added at lowest priority.

We used the GMOS R150 grating + the GG455 filter in order obtain spectra with about 4600 – 9000 Å wavelength coverage. This was designed to cover the [OII] 3727 emission line expected at $\sim$ 6300 Å, given the photo-z estimate of $\sim$ 0.7 for the arcs as well as the Mg absorption features at $\sim$ 7000 Å (and the 4000 Å break at $\sim$ 5600 Å) for the $z \sim 0.4$ cluster elliptical galaxies.

We used 2 MOS masks in order to fully target these cluster galaxies (along with the arcs) for spectroscopy. Each mask had a 3600 second exposure time split into 4 900-second exposures for cosmic ray removal. We also took standard Cu-Ar lamp spectra for wavelength calibrations and standard star spectra for flux calibrations. All data were taken in queue observing mode. A summary of the observations is given in Table 1.

3.1. Data Reduction

The BCS imaging data were processed using the Dark Energy Survey data management system (DESDM V3) which is under development at UIUC/NCSA/Fermilab (Mohr et al. 2008; Ngeow et al. 2006; Zenteno et al. 2011). The images are corrected for instrumental effects which include crosstalk correction, pupil ghost correction, overscan correction, trimming, bias subtraction, flat fielding and illumination correction. The images are then astrometrically calibrated and remapped for later coaddition. For photometric data, a photometric calibration is applied to the single-epoch and coadd object photometry. The Astr$\mathcal{O}$matic software[1] SExtractor (Bertin & Arnouts 1996), SCAMP (Bertin 2006) and SWarp (Bertin et al. 2002) are used for cataloging, astrometric refinement and remapping for coaddition over each image. We have used the coadded images in the *griz* bands for this analysis.

The spectroscopic data were processed using the standard data reduction package provided by Gemini that runs in the IRAF framework[2]. We used version 1.9.1. This produced

[1]http://www.astromatic.net

[2]http://www.gemini.edu/sciops/data-and-results/processing-software

flux- and wavelength-calibrated 1-D spectra for all the objects. Additional processing for the source spectra was done using the IRAF task `apall`.

3.2. Cluster properties

We adopt the procedure used by the maxBCG cluster finder (Koester et al. 2007a,b) to determine cluster membership and cluster richness and to derive a richness-based cluster mass estimate. We first measure N_{gal}, the number of cluster red sequence galaxies, within a radius 1 h^{-1} Mpc ($= 4.55'$) of the BCG, that are also brighter than $0.4L_*$ at the cluster redshift $z = 0.38$. From Koester et al. (2007a), $0.4L_*$ corresponds to an i-band absolute magnitude $M = -20.25 + 5 \log h$ at $z = 0$, while at $z = 0.38$, $0.4L_*$ corresponds to an apparent magnitude $i = 20.5$ (specific value provided by J. Annis & J. Kubo, private communication), after accounting for both K-correction and evolution (also as described in Koester et al. 2007a). We apply this magnitude cut using the SExtractor i-band `MAG_AUTO` magnitude, which provides a measure of a galaxy's total light. (Note the $3''$-diameter aperture magnitude used earlier for target selection in general measures less light cf. `MAG_AUTO`, but is better suited for roughly approximating the light entering a GMOS slit.) We set the red sequence membership cuts to be $g - r$ and $r - i$ color both within 2σ of their respective central values $(g - r)_0 = 1.77$ and $(r - i)_0 = 0.65$, where the latter are determined empirically based on the peaks of the color histograms of galaxies within 1 h^{-1} Mpc of the BCG. In applying the color cuts we use the colors defined by SExtractor $3''$-diameter aperture magnitudes (this provides higher S/N colors compared to using `MAG_AUTO`), and for the uncertainty we define $\sigma = \sqrt{\sigma_{color}^2 + \sigma_{intrinsic}^2}$, where σ_{color} is the color measurement error derived from the SExtractor aperture magnitude errors, and $\sigma_{intrinsic}$ is the intrinsic red sequence color width, taken to be 0.05 for $g - r$ and 0.06 for $r - i$ (Koester et al. 2007a).

Carrying out the above magnitude and color cuts, we obtain an initial richness estimate $N_{gal} = 44$. Then, as discussed in Hansen et al. (2005), we define another radius $r_{200}^{gal} = 0.156\ N_{gal}^{0.6}\ h^{-1}$ Mpc $= 1.51\ h^{-1}$ Mpc ($= 6.88'$), and repeat the same cuts within r_{200}^{gal} of the BCG to obtain a final richness estimate $N_{200} = 55$. Finally, using the weak lensing mass calibration of Johnston et al. (2007) for maxBCG clusters, we obtain a mass estimate $M_{200} = (8.794 \times 10^{13}) \times (N_{200}/20)^{1.28}\ h^{-1}\ M_{\odot} = (4.6 \pm 2.1) \times 10^{14}\ M_{\odot}$ ($h = 0.7$), where we have also adopted the fractional error of 0.45 derived by Rozo et al. (2009) for this N_{200}-based estimate of M_{200} for maxBCG clusters.

We note that Rozo et al. (2010) apply a factor of 1.18 to correct the Johnston et al. (2007) cluster masses upward, in order to account for a photo-z bias effect that is detailed in Mandelbaum et al. (2008). We have not applied this correction as it makes only a 0.4σ

difference, although we remark that the resulting mass $M_{200} = 5.4 \times 10^{14}\ M_{\odot}$ does appear to improve the (already good) agreement with our other mass estimates below (see §3.4 and §6.1).

Fig. 3 shows color-magnitude and color-color plots of all galaxies that have $i < 21$ (SExtractor `MAG_AUTO`) and that are within a radius $r_{200}^{gal} = 1.51\ h^{-1}$ Mpc ($= 6.88'$) of the BCG. Note we have extended the magnitude limit here down to $i = 21$, to match the effective magnitude limit of our spectroscopic redshift sample (§3.3 below) In particular, we find 86 maxBCG cluster members for $i < 21$, compared to the earlier $N_{200} = 55$ for $i < 20.5$ (corresponding to $0.4L_*$). These member galaxies are shown using red symbols in Fig. 3 and their properties are given in Table 3.

3.3. Redshift determinations

The redshift extraction was carried out using the `xcsao` and `emsao` routines in the IRAF external package `rvsao` (Kurtz & Mink 1998). We obtained spectra for the 55 objects that were targeted. Four of these spectra were of the source. Out of the remaining 51 spectra we had sufficient signal-to-noise in 42 of them to determine a redshift. Thirty of the objects with redshifts between 0.377 and 0.393 constitute our spectroscopic sample of cluster galaxies. Fig. 4 shows the spatial distribution of galaxies within a $6' \times 6'$ box centered on the BCG, with maxBCG cluster members, arc knots, and objects with spectroscopic redshifts indicated by different colors and symbols. Table 3 summarizes the properties of the 30 cluster member galaxies with redshifts, and Table 4 summarizes the properties of the remaining 12 spectroscopic non-member galaxies. In Fig. 5 we show four examples of the flux-calibrated cluster member spectra including the BCG.

Examination of Table 3 and Table 4 shows that our spectroscopic sample is effectively limited at $i \approx 21$, as 39 of the 42 non-arc redshifts have $i < 21$. Note that of the 30 spectroscopically defined cluster members, 22 are also maxBCG members, while another 7 lie close to the maxBCG color selection boundaries. Also, of the 12 spectroscopic non-members, none meets the maxBCG criteria except the faintest one (with $i = 21.58$).

The redshift of the source was determined from a single emission line at 7100Å which is present with varying signal-to-noise in each of the knots that were observed. We take this line to be the [OII]3727Å line which yields a redshift of 0.9057 ± 0.0005. The four flux-calibrated source spectra are shown in Fig. 6. Knot A2 was observed under seeing conditions that were a factor of two worse than for the other three knots (see Table 1).

3.4. Velocity dispersion and cluster mass measurement

We used the 30 cluster galaxies to estimate the redshift and velocity dispersion of the cluster using the biweight estimators of Beers et al. (1990). We first use the biweight location estimator to determine the best estimate for cz. This yields a value of $cz = 115151.1 \pm 241.1$ km s^{-1} which translates to a redshift of $z_c = 0.3838 \pm 0.0008$. We then use this estimate of the cluster redshift to determine the peculiar velocity v_p for each cluster member relative to the cluster center of mass using

$$v_p = \frac{(cz - cz_c)}{(1 + z_c)} \tag{1}$$

We determine the biweight estimate of scale for v_p which is equal to the velocity dispersion of the cluster. We find a value for the velocity dispersion of $\sigma_c = 855^{+108}_{-96}$ km s^{-1}. The uncertainties are obtained by doing a jackknife resampling. The redshift distribution is shown in Fig. 7. The overlaid Gaussian has a mean of z_c and a width of $\sigma_c \times (1 + z_c)$. The lines represent the individual peculiar velocities v_p of the cluster members.

We can use the estimated velocity dispersion to derive an estimate for the cluster mass. We use the results of Evrard et al. (2008) (see also Becker et al. 2007) which relates M_{200} to the dark matter velocity dispersion

$$M_{200} = 10^{15}\ M_\odot \frac{1}{h(z)} \left(\frac{\sigma_{DM}}{\sigma_{15}}\right)^{1/\alpha} , \tag{2}$$

where $h(z) = H(z)/100$ km s^{-1}Mpc^{-1} is the dimensionless Hubble parameter. The values of the parameters were found to be $\sigma_{15} = 1082.9 \pm 4$ km s^{-1} and $\alpha = 0.3361 \pm 0.0026$ (Evrard et al. 2008). Using the standard definition of velocity bias $b_v = \sigma_{gal}/\sigma_{DM}$, where σ_{gal} is the galaxy cluster velocity dispersion, we can rewrite Equation 2 as

$$b_v^{1/\alpha} M_{200} = 10^{15}\ M_\odot \frac{1}{h(z)} \left(\frac{\sigma_{gal}}{\sigma_{15}}\right)^{1/\alpha} , \tag{3}$$

where the quantity $b_v^{1/\alpha} M_{200}$ parameterizes our lack of knowledge about velocity bias. Substituting in the measured values for σ_{gal} we obtain $b_v^{1/\alpha} M_{200} = 5.79^{+2.22}_{-1.99} \times 10^{14} M_\odot$.

Bayliss et al. (2010, and references therein) discuss an "orientation bias" effect which causes an upward bias in the measured velocity dispersions of lensing-selected clusters, due to the higher likelihood of the alignment along the line of sight of the major axes of the cluster halos, which are in general triaxial. Bayliss et al. (2010) estimate that on average this will result in the dynamical mass estimate being biased high by 19-20%, using the same relation between M_{200} and velocity dispersion as we have used (Eqn. 2 above; Evrard et al.

2008). Correcting for this orientation bias effect would result in $b_v^{1/\alpha} M_{200} = 4.8 \times 10^{14} M_\odot$, which is not a significant difference, as the change is well under 1σ. We therefore do not apply this correction, but we do note that it would improve the already good agreement with our other mass estimates in §3.2 and §6.1 (assuming no velocity bias, $b_v = 1$.)

4. Strong Lensing Properties

We use the coadded r-band image shown in Fig. 8 to study the strong lensing features of the system as it has the best seeing and hence shows the most detail. To remove the contribution to the arc fluxes from nearby objects we used GALFIT (Peng et al. 2002) to model the profiles of these objects (galaxies and stars) and then subtracted the model from the image. This was done for all four bands $griz$. These subtracted images are used for all determinations of arc fluxes and positions. A number of individual knots can be observed in the system along with the more elongated features. For example it appears that knot A1 is actually composed of two individual bright regions which are resolved by the Sextractor object extraction described below. Knot A2 also appears to have two components although these are not resolved by the object extraction so we treat them as one in the modeling. Even though the cluster is fairly massive we do not see evidence for additional arc-like features outside of the central circular feature. In this case we expect the mass of the lens to be well constrained by the image positions.

We use the criteria that to obtain multiple images the average surface mass density within the tangential critical curve must equal the critical surface mass density Σ_{crit}. The tangentially oriented arcs occur at approximately the tangential critical curves and so the radius of the circle θ_{arc} traced by the arcs provides a measurement of the Einstein radius θ_{EIN} (Narayan & Bartelmann 1996). The mass M_{EIN} enclosed with the Einstein radius is therfore given by

$$M_{EIN} = \Sigma_{crit} \pi (D_l \theta_{EIN})^2 \tag{4}$$

Substituting for Σ_{crit} gives

$$M_{EIN} = \frac{c^2}{4G} \frac{D_l D_s}{D_{ls}} \theta_{EIN}^2 \tag{5}$$

where D_s is the angular diameter distance to the source, D_l the angular diameter distance to the lens, and D_{ls} the angular diameter distance between the lens and the source. These values are $D_s = 1610$ Mpc, $D_l = 1081$ Mpc and $D_{ls} = 825$ Mpc.

To determine the Einstein radius we ran Sextractor (Bertin & Arnouts 1996) on the r-band image. This identified eight distinct objects in the image. We used the coordinates of those eight objects and fit them to a circle. The radius of the circle gives us a measure of the

Einstein radius. The Einstein radius we measure is $\theta_{EIN} = 7.53 \pm 0.25''$ which translates to 39.5 ± 1.3 kpc. This yields a mass estimate of $(1.5 \pm 0.1) \times 10^{13} M_\odot$ and a corresponding velocity dispersion (assuming an isothermal model for the mass distribution) of $\sigma = 694 \pm 12$ km s^{-1}.

The magnification of the lens f_{lens} can be roughly estimated under the assumption that the 1/2-light radius of a source at redshift $z \sim 0.9$ is about $0.46''$ (derived from the mock galaxy catalog described in Jouvel et al. (2009)). The ratio of the area subtended by the ring to that subtended by the source is $\sim 0.6 \times (4R/\delta r)$, where R is the ring radius and δr is the 1/2-light radius of the source. The 0.6 factor accounts for the fraction of the ring that actually contains images. This gives a magnification of $f_{lens} = 39$.

To obtain a more quantitative value for the magnification we have used the `PixeLens`[3] program (Saha & Williams 2004) to model the lens. `PixeLens` is a parametric modeling program that reconstructs a pixelated mass map of the lens. It uses as input the coordinates of the extracted image positions and their parities along with the lens and source redshifts. It samples the solution space using a Markov Chain Monte Carlo method and generates an ensemble of mass models that reproduce the image positions. We used the Sextractor image positions obtained above and assigned the parities according to the prescription given in Read (2007). In Saha & Williams (2004) they note that if one uses pixels that are too large then the mass distribution is poorly resolved and not enough steep mass models are allowed. We have chosen a pixel size such that this should not be a problem.

It is well known (see for example Saha & Williams (2006)) that changing the slope of the mass profile changes the overall magnification, in particular a steeper slope produces a smaller magnification but does not change the image positions. Therefore the quoted magnification should be taken as a representative example rather than a definitive answer. The magnification quoted is the sum over the average values of the magnification for each image position for 100 models. We obtain a value of $f_{lens} = 141 \pm 39$ where the error is the quadrature sum of the RMS spreads of the individual image magnifications. `PixeLens` can also determine the enclosed mass within a given radius. For the 100 models we obtain $M_{EIN} = (1.4 \pm 0.02) \times 10^{13} M_\odot$ which is within 1σ of the mass obtained from the circle fit described above.

In order to combine the strong lensing mass with the mass estimate from the weak lensing analysis (in §6.1 below) we will need to estimate the mass within θ_{EIN} that is due to dark matter alone (M_{DM}). To do this we will need to subtract estimates of the stellar mass (M_S) and the hot gas mass (M_G) from the total mass M_{EIN}. To determine M_S we use the GALAXEV (Bruzual & Charlot 2003) evolutionary stellar population synthesis code to fit

[3]Version 2.17: http://www.qgd.uzh.ch/programs/pixelens/

galaxy spectral energy distribution models to the *griz* magnitudes of the BCG within the Einstein radius. The BCG photometric data are taken from the GALFIT modeling described above, and we sum up the light of the PSF-deconvolved GALFIT model inside the Einstein radius. The GALAXEV models considered are simple stellar population (SSP) models which have an initial, instantaneous burst of star formation; such models provide good fits to early-type galaxies, such as those in clusters. In particular we find a good fit to the BCG, using a SSP model with solar metallicity, a Chabrier (2003) stellar initial mass function (IMF), and an age 9.25 Gyr (this age provided the best χ^2 over the range we considered, from 1 Gyr to 9.3 Gyr, the latter being the age of the universe for our cosmology at the cluster redshift $z = 0.38$). The resulting stellar mass (more precisely the total stellar mass integrated over the IMF) is $M_S = 1.7 \times 10^{12} M_{\odot}$.

To estimate the gas mass M_G we have looked at estimates of hot gas fraction f_{gas} in cluster cores from X-ray observations. Typical f_{gas} measurements are of order 10% (Maughan et al. 2004; Pointecouteau et al. 2004) which give us an M_G estimate of $1.5 \times 10^{12} M_{\odot}$.

Finally we calculate the *total* M/L ratio within θ_{EIN} for the i-band. This yields a value of $(M/L)_i = 33.7 \pm 4.4\ (M/L)_{\odot}$.

5. Weak Lensing Measurements

5.1. Adaptive Moments

We used the program Ellipto (Smith et al. 2001) to compute adaptive moments (Bernstein & Jarvis 2002; Hirata et al. 2004) of an object's light distribution, i.e., moments optimized for signal-to-noise via weighting by an elliptical Gaussian function self-consistently matched to the the object's size. Ellipto computes adaptive moments using an iterative method and runs off of an existing object catalog produced by SExtractor for the given image. Ellipto is also a forerunner of the the adaptive moments measurement code used in the SDSS photometric processing pipeline Photo.

We ran Ellipto on our coadded BCS images and corresponding SExtractor catalogs, doing so independently in each of the *griz* filters to obtain four separate catalogs of adaptive second moments:

$$Q_{xx} = \int x^2\ w(x,y) I(x,y)\ dxdy \Big/ \int w(x,y) I(x,y)\ dxdy \quad (6)$$

$$Q_{yy} = \int y^2\ w(x,y) I(x,y)\ dxdy \Big/ \int w(x,y) I(x,y)\ dxdy \quad (7)$$

$$Q_{xy} = \int xy\ w(x,y)I(x,y)\ dxdy \Big/ \int w(x,y)I(x,y)\ dxdy \ , \tag{8}$$

where $I(x,y)$ denotes the measured counts of an object at position x,y on the CCD image, and $w(x,y)$ is the elliptical Gaussian weighting function determined by Ellipto. The images are oriented with the usual convention that North is up and East is to the left, i.e., right ascension increases along the $-x$ direction and declination increases along the $+y$ direction. We then computed the ellipticity components e_1 and e_2 of each object using one of the standard definitions

$$e_1 = (Q_{xx} - Q_{yy})/(Q_{xx} + Q_{yy}) \tag{9}$$

$$e_2 = 2Q_{xy}/(Q_{xx} + Q_{yy}) \ . \tag{10}$$

5.2. PSF Modeling

For each filter, we then identified a set of bright but unsaturated stars to use for PSF fitting. We chose the stars from the stellar locus on a plot of the size measure $Q_{xx} + Q_{yy}$ from Ellipto vs. the magnitude `MAG_AUTO` from SExtractor, using simple cuts on size and magnitude to define the set of PSF stars. We then derived fits of the ellipticities e_1, e_2 and the size $Q_{xx} + Q_{yy}$ of the stars vs. CCD x and y position, using polynomial functions of cubic order in x and y (i.e., the highest order terms are x^3, x^2y, xy^2, and y^3). On each image, these fits were done separately in each of 8 rectangular regions, defined by splitting the image area into 2 parts along the x direction and into 4 parts along the y direction, corresponding to the distribution of the 8 Mosaic-II CCDs over the image. This partitioning procedure was needed in order to account for discontinuities in the PSF ellipticity and/or size as we cross CCD boundaries in the Mosaic-II camera. Also note that the individual exposures comprising the final coadded image in each filter were only slightly dithered, so that the CCD boundaries were basically preserved in the coadd. To illustrate the PSF variation in our images, we present in Figure 9 "whisker plots" that show the spatial variation of the magnitude and orientation of the PSF ellipticity across our i- and r-band images . In addition, we also show the residuals in the PSF whiskers remaining after our fitting procedure, showing that the fits have done a good job of modeling the spatial variations of the PSF in our data.

We next used our PSF model to correct our galaxy sizes and ellipticities for the effects of PSF convolution. Specifically, for the size measure $Q_{xx} + Q_{yy}$ we used the simple relation (cf. Hirata & Seljak 2003)

$$Q_{xx,true} + Q_{yy,true} = (Q_{xx,observed} + Q_{yy,observed}) - (Q_{xx,PSF} + Q_{yy,PSF}) \tag{11}$$

to estimate the true size $Q_{xx,true} + Q_{yy,true}$ of a galaxy from its observed size $Q_{xx,observed} + Q_{yy,observed}$, where $Q_{xx,PSF} + Q_{yy,PSF}$ is obtained from the PSF model evaluated at the x, y position of the galaxy. For the ellipticities we similarly used the related expressions

$$e_{i,true} = \frac{e_{i,observed}}{R_2} + \left(1 - \frac{1}{R_2}\right) e_{i,PSF} \ , \ \ i = 1, 2 \tag{12}$$

$$R_2 \equiv 1 - \frac{Q_{xx,PSF} + Q_{yy,PSF}}{Q_{xx,observed} + Q_{yy,observed}} \tag{13}$$

The relations used in this simple correction procedure strictly hold only for unweighted second moments, or for adaptive moments in the special case when both the galaxy and the PSF are Gaussians. We have therefore also checked the results using the more sophisticated "linear PSF correction" procedure of Hirata & Seljak (2003), which uses additional fourth order adaptive moment measurements (also provided here by Ellipto) in the PSF correction procedure. In particular, the linear PSF correction method is typically applied in weak lensing analyses of SDSS data. However, we found nearly indistinguishable tangential shear profiles from applying the two PSF correction methods, and we therefore adopted the simpler correction method for our final results.

5.3. Shear Profiles and Mass Measurements

Given the estimates of the true galaxy ellipticities from Equation (12), we then computed the tangential (e_T) and B-mode or cross ($e_\times$) ellipticity components, in a local reference frame defined for each galaxy relative to the BCG:

$$e_T = e_1 \cos(2\phi) - e_2 \sin(2\phi) \tag{14}$$

$$e_\times = e_1 \sin(2\phi) + e_2 \cos(2\phi) \tag{15}$$

where ϕ is the position angle (defined West of North) of a vector connecting the BCG to the galaxy in question. Here we have dropped the subscript *true* for brevity. The ellipticities were then converted to shears γ using $\gamma = e/R$, where R is the responsivity, for which we adopted the value $R = 2(1 - \sigma_{SN}^2) = 1.73$, using $\sigma_{SN} = 0.37$ as the intrinsic galaxy shape noise as done in previous SDSS cluster weak lensing analyses (e.g., Kubo et al. 2007, 2009).

We then fit our galaxy shear measurements to an NFW profile by minimizing the following expression for χ^2:

$$\chi^2 = \sum_{i=1}^{N} \frac{[\gamma_i - \gamma_{NFW}(r_i; M_{200}, c_{200})]^2}{\sigma_\gamma^2} \tag{16}$$

where the index i refers to each of the N galaxies in a given sample, r_i is a galaxy's projected physical radius from the BCG (at the redshift of the cluster), σ_γ is the measured standard deviation of the galaxy shears, and γ_{NFW} is the shear given by Equations (14-16) of Wright & Brainerd (2000) for an NFW profile with mass M_{200} and concentration c_{200}. We used a standard Levenberg-Marquardt nonlinear least-squares routine to minimize χ^2 and obtain best-fitting values and errors for the parameters M_{200} and c_{200} of the NFW profile. Similar fits of the weak lensing radial shear profile to a parameterized NFW model have often been used to constrain the mass distributions of galaxy clusters (e.g., King & Schneider 2001; Clowe & Schneider 2001; Kubo et al. 2009; Oguri et al. 2009; Okabe et al. 2010). Note that we chose the above expression for χ^2 since it does *not* require us to do any binning in radius, but for presentation purposes below we will have to show binned radial shear profiles compared to the NFW shear profiles obtained from our binning-independent fitting method.

For the shear fitting analysis, we defined galaxy samples separately in each of the four *griz* filters using cuts on the magnitude `MAG_AUTO` and on the size $Q_{xx,observed} + Q_{yy,observed}$, as detailed in Table 5. The bright magnitude cut was chosen to exclude brighter galaxies which would tend to lie in the foreground of the cluster and hence not be lensed, while the faint magnitude cuts were set to the photometric completeness limit in each filter, as defined by the turnover magnitude in the histogram of SExtractor `MAG_AUTO` values. For the size cut, we set it so that only galaxies larger than about 1.5 times the PSF size would be used, as has been typically done in SDSS cluster weak lensing analyses (e.g., Kubo et al. 2007, 2009). Note that in order to properly normalize the NFW shear profile to the measurements, we also need to calculate the critical surface mass density Σ_{crit}, which depends on the redshifts of the lensed source galaxies as well as the redshift of the lensing cluster; see Equations (9,14) of Wright & Brainerd (2000). To do this, we did not use any individual redshift estimates for the source galaxies in our analysis, but instead we calculated an effective value of $1/\Sigma_{crit}$ via an integral over the source galaxy redshift distribution published for the Canada-France-Hawaii Telescope Legacy Survey (CFHTLS; Ilbert et al. 2006), as appropriate to the magnitude cuts we applied in each of the *griz* filters.

Our NFW fitting results are shown in Figures 10-11 and detailed in Table 5. We show results for both the tangential and B-mode shear components. As lensing does not produce an B-mode shear signal, these results provide a check on systematic errors and should be consistent with zero in the absence of significant systematics. For all of our filters, our B-mode shear results are indeed consistent with no detected mass, as the best-fit M_{200} is within about 1σ of zero. On the other hand, for the tangential shear results in the r, i, and z filters, we do indeed obtain detections of non-zero M_{200} at the better than 1.5σ level. In the g filter we do not detect a non-zero M_{200}. Comparing the weak lensing results from the different filters serves as a useful check of the robustness of our lensing-based cluster mass measurement, in particular as the images in the different filters are subject to quite different PSF patterns, as shown earlier in Fig. 9. Though the mass errors are large, the M_{200} values from the r-, i-, and z-band weak lensing NFW fits are nonetheless consistent with each other and with the masses derived earlier from the velocity dispersion and maxBCG richness analyses. Moreover, independent of the NFW fits, we have also derived probabilities (of exceeding the observed χ^2) that our *binned* shear profiles are consistent with the null hypothesis of zero shear. As shown in Table 5, we see that the B-mode profiles are in all cases consistent with zero, as expected, but that the tangential profiles for the r and i filters are not consistent with the null hypothesis at about the 2σ level (probabilities ≈ 0.06), thus providing model-independent evidence for a weak lensing detection of the cluster mass.

5.4. Combining Weak Lensing Constraints from Different Filters

Here we will combine the weak lensing shear profile information from the different filters $griz$ in order to improve the constraints on the NFW parameters, in particular on M_{200}. The main complication here is that although the ellipticity measurement errors are independent among the different filters, the most important error for the shear measurement is the intrinsic galaxy shape noise, which is correlated among filters because a subset of the galaxies is common to two or more filters, and for these galaxies we expect their shapes to be fairly similar in the different filters. In particular we find that the covariance of the true galaxy ellipticities between filters is large, for example, the covariance of e_1 between the i and r filters, $\mathrm{Cov}(e_{1,i}, e_{1,r}) = \frac{1}{N}\sum(e_{1,i} - \bar{e}_{1,i})(e_{1,r} - \bar{e}_{1,r})$, is about 0.9 times the variance of e_1 in the i and r filters individually. The same holds true for e_2 and for the other filters as well. We will not attempt to use a full covariance matrix approach to deal with the galaxy shape correlations when we combine the data from two or more filters. Instead, we take a simpler approach of scaling the measured standard deviation of the shear (the σ_γ used to calculate χ^2 in Equation 16) by $\sqrt{N/N_{unique}}$, where N is the total number of galaxies in a given multi-filter sample, and N_{unique} is the number of unique galaxies in the same sample. This is equivalent to rescaling χ^2 in the NFW fit to correspond to N_{unique} degrees of freedom instead of N. We have verified using least-squares fits to Monte Carlo simulations of NFW shear profiles that this simple approach gives the correct fit uncertainties on M_{200} and c_{200} when the mock galaxy data contain duplicate galaxies, with identical e_1 and e_2 values, simulating the case of *completely* correlated intrinsic galaxy shapes among filters. Note that our approach is conservative and will slightly overestimate the errors, because the galaxy shapes in the real data are about 90% correlated, not fully correlated, among filters.

Before fitting the combined shear data from multiple filters, we make one additional multiplicative rescaling of the shear values, so that all filters will have the same effective value of $1/\Sigma_{crit}$, corresponding to a fiducial effective source redshift $z_{crit} = 0.7$. This correction is small, with the largest being a factor of 1.18 for the z-band data. The results of the NFW fits for the multi-filter samples are given in Table 5, where we have tried the filter combinations $i+r$, $i+r+z$, and $i+r+z+g$. We see that these multi-filter samples all provide better fractional errors on M_{200} compared to those from the single-filter data. Also, as expected, the B-mode results in all cases are consistent with no detected M_{200} and zero shear. For our final weak lensing results, we adopt the NFW parameters from the $i+r+z$ sample, as it provides the best fractional error ($\sigma_{M_{200}}/M_{200} \approx 0.5$) on M_{200}; we obtain $M_{200} = 5.0^{+2.9}_{-2.3} \times 10^{14}$ solar masses, and $c = 4.9^{+3.9}_{-2.2}$. Figure 12 shows the shear profile data and best fit results for the $i+r+z$ sample. This final weak lensing value for M_{200} agrees well with the earlier values of M_{200} derived from the cluster galaxy velocity dispersion (assuming no velocity bias) and from the cluster richness N_{200}.

6. Combined Constraints on Cluster Mass and Concentration

6.1. Combining Strong and Weak Lensing

In this section we combine the strong lensing and weak lensing information together in order to further improve our constraints on the NFW profile parameters, in particular on the concentration parameter c_{200}. The addition of the strong lensing information provides constraints on the mass within the Einstein radius, close to the cluster center, thereby allowing us to better measure the central concentration of the NFW profile and improve the uncertainties on the concentration c_{200}. Oguri et al. (2009) incorporated the strong lensing information in the form of a constraint on the Einstein radius due to just the dark matter distribution of the cluster, and they specifically excluded the contribution of (stellar) baryons to the Einstein radius. Their intent, as well as ours in this paper (§ 6.2), is to compare the observed cluster NFW concentration to that predicted from dark-matter-*only* simulations. Thus the contribution of baryonic matter should be removed, most importantly in the central region within the Einstein radius, where baryonic effects are the largest due in particular to the presence of the BCG. In practice with the present data we can do this separation of the baryonic contribution only for the strong lensing constraint, and strictly speaking the weak lensing profile results from the total mass distribution rather than from dark matter alone.

Here we combine the strong and weak lensing data using an analogous but somewhat simpler method compared to that of Oguri et al. (2009), specifically by adding a second term to χ^2 (Equation 16) that describes the constraint on the dark matter (only) mass within the observed Einstein radius:

$$\chi^2 = \sum_{i=1}^{N} \frac{[\gamma_i - \gamma_{NFW}(r_i; M_{200}, c_{200})]^2}{\sigma_\gamma^2} + \frac{[M_{DM}(< \theta_E) - M_{NFW}(< \theta_E; M_{200}, c_{200})]^2}{\sigma^2_{M_{DM}(<\theta_E)}} \quad (17)$$

where $\theta_E = 7.53''$ is the observed Einstein radius due to the *total* cluster mass distribution, $M_{DM}(< \theta_E)$ is the dark matter (only) mass within θ_E, and $M_{NFW}(< \theta_E; M_{200}, c_{200})$ is the mass within θ_E of an NFW profile with mass M_{200}, concentration c_{200}, redshift $z = 0.38$, and source redshift $z = 0.9057$. $M_{NFW}(< \theta_E; M_{200}, c_{200})$ is derived based on Equation (13) of Wright & Brainerd (2000). As obtained earlier in §4, we estimate $M_{DM}(< \theta_E)$ by subtracting estimates of the stellar mass and hot gas mass from the total mass within θ_E, obtaining $M_{DM}(< \theta_E) = (1.18 \pm 0.2) \times 10^{13} M_\odot$ when subtracting off both stellar and gas mass, or $M_{DM}(< \theta_E) = (1.33 \pm 0.2) \times 10^{13} M_\odot$ when subtracting off only stellar mass. The former is our best estimate of $M_{DM}(< \theta_E)$, while the latter serves as an upper limit on $M_{DM}(< \theta_E)$ and hence on the best-fit concentration c_{200}. We also conservatively estimate the error on $M_{DM}(< \theta_E)$ to be one of the stellar mass/gas mass components added in quadrature to the uncertainty on the total M_{EIN} from §4.

We apply the combined strong plus weak lensing analysis to our best weak lensing sample, the multi-filter $i + r + z$ data set. The fit results are given in Table 5 and shown in Figure 12. We find $M_{200} = 4.9^{+2.9}_{-2.2} \times 10^{14}$ solar masses, nearly identical to the final weak lensing result. We also get a concentration $c_{200} = 5.5^{+2.7}_{-1.6}$, again consistent with the final weak lensing fit, but with a 30% improvement in the error on c_{200}, demonstrating the usefulness of adding the strong lensing information to constrain the NFW concentration. Using the upper limit $M_{DM}(< \theta_E)$ value (with only stellar mass subtracted) gives nearly the same $M_{200} = 4.8^{+2.8}_{-2.2} \times 10^{14} M_\odot$, while the resulting NFW concentration is higher, as expected, with $c_{200} = 6.2^{+3.2}_{-1.7}$, but still consistent with the fit using our best estimate of $M_{DM}(< \theta_E)$.

6.2. Combining Lensing, Velocity Dispersion and Richness Constraints

In the above sections we have obtained quite consistent constraints on the cluster mass M_{200} using three independent techniques: (1) $M_{200}(\text{lensing}) = 4.9^{+2.9}_{-2.2} \times 10^{14} M_\odot$ from combined weak + strong lensing (§6.1); (2) $M_{200}(\sigma_c) = 5.79^{+2.22}_{-1.99} \times 10^{14} M_\odot$ from the cluster galaxy velocity dispersion σ_c (§3.4; assuming no velocity bias, $b_v = 1$); and (3) $M_{200}(N_{200}) = (4.6 \pm 2.1) \times 10^{14} M_\odot$ from the maxBCG-defined cluster richness N_{200} (§3.2). We note that these methods are subject to different assumptions and systematic errors. For example, the velocity dispersion based mass estimate assumes the cluster is virialized, an assumption supported by the Gaussian-shaped velocity distribution of the cluster members shown in Fig. 7. Also, the richness based mass estimate relies on the N_{200}-M_{200} calibration (Johnston et al. 2007) obtained for SDSS maxBCG clusters at lower redshifts $z = 0.1 - 0.3$ and assumes that this calibration remains valid for our cluster at $z = 0.38$. It is encouraging that we are obtaining a cluster mass measurement that appears to be robust to these disparate assumptions and that shows good agreement among multiple independent methods.

We will therefore combine the results from the different techniques in order to obtain final constraints on M_{200} and concentration c_{200} that are significantly improved over what any one technique permits. Specifically, we can add the M_{200} constraints from the velocity dispersion and richness measurements as additional terms to the weak + strong lensing χ^2 (Equation 17):

$$\chi^2 = \sum_{i=1}^{N} \frac{[\gamma_i - \gamma_{NFW}(r_i; M_{200}, c_{200})]^2}{\sigma_\gamma^2} + \frac{[M_{DM}(<\theta_E) - M_{NFW}(<\theta_E; M_{200}, c_{200})]^2}{\sigma^2_{M_{DM}(<\theta_E)}} + \frac{[M_{200}(\sigma_c) - M_{200}]^2}{\sigma^2_{M_{200}(\sigma_c)}} + \frac{[M_{200}(N_{200}) - M_{200}]^2}{\sigma^2_{M_{200}(N_{200})}} \quad (18)$$

Minimizing this overall χ^2 results in the final best-fitting NFW parameters $M_{200} = 5.1^{+1.3}_{-1.3} \times 10^{14} M_\odot$ and $c_{200} = 5.4^{+1.4}_{-1.1}$. These results are consistent with the final lensing-based values $M_{200}(\text{lensing}) = 4.9^{+2.9}_{-2.2} \times 10^{14} M_\odot$ and $c_{200}(\text{lensing}) = 5.5^{+2.7}_{-1.6}$, but have errors nearly a factor of two smaller. Note these quoted errors are 1-parameter, 1σ uncertainties; we plot the joint 2-parameter, 1σ and 2σ contours in Fig. 13.

We also note that for the three methods weak lensing, velocity dispersion, and cluster richness, the corresponding NFW parameters result from the the *total* mass distribution, consisting of both dark matter and baryonic (stellar plus hot gas) components. Dark matter is dominant over the bulk of the cluster, while baryons can have a significant effect in the cluster core (e.g., Oguri et al. 2009). As described earlier (§ 6.1), we have thus subtracted off the baryonic contribution to the strong lensing constraint as the intent is to compare (see below) our cluster concentration value against those from dark-matter-only simulations. Note that we have not isolated the dark matter contribution for the other three methods and cannot easily do so. For weak lensing, the shear profile is sensitive to the total mass distribution, not just to dark matter. For the velocity dispersion method, the galaxies act as test particles in the overall cluster potential, which is due, again, to both dark matter and baryons. For the cluster richness method, the Johnston et al. (2007) N_{200}-M_{200} relation we use was derived from stacked cluster weak lensing shear profile fits, including a BCG contribution but otherwise no other baryonic components; thus again the M_{200} value is essentially for the total mass distribution. Nonetheless, the bulk of the baryonic contribution is in the cluster core and is accounted for via the strong lensing constraint, so we expect the comparison below of our cluster concentration value to those of dark matter simulations to be a reasonable exercise.

Recent analyses (e.g., Oguri et al. 2009; Broadhurst & Barkana 2008) of strong lensing clusters have indicated that these clusters are more concentrated than would be expected from ΛCDM predictions, though others have argued that no discrepancy exists if baryonic effects are accounted for (Richard et al. 2010). In the former case, Oguri et al. (2009) found a concentration $c_{\rm vir} \approx 9$ for the 10 strong lensing clusters in their analysis sample, compared to a value of $c_{\rm vir} \approx 6$ expected for strong-lensing-selected clusters or $c_{\rm vir} \approx 4$ for clusters overall (e.g., Broadhurst & Barkana 2008; Oguri & Blandford 2009). We illustrate these different concentration values in Fig. 13. We use Eqn. (17) of Oguri et al. (2009), $\bar{c}_{\rm vir}({\rm sim}) = \frac{7.85}{(1+z)^{0.71}}(M_{\rm vir}/2.78 \times 10^{12} M_\odot)^{-0.081}$, which comes from the ΛCDM N-body simulations of Duffy et al. (2008), to show the typical concentration of clusters overall, and multiply by a factor of 1.5 (Oguri et al. 2009) to show the higher concentration expected for lensing selected clusters. We also use Eqn. (18) of Oguri et al. (2009), $\bar{c}_{\rm vir}({\rm fit}) = \frac{12.4}{(1+z)^{0.71}}(M_{\rm vir}/10^{15} M_\odot)^{-0.081}$, to show the fit results for their cluster sample. In these relations, we set $z = 0.4$ to match the redshift of our cluster. Moreover, we convert from the $M_{\rm vir}, c_{\rm vir}$ convention used by Oguri et al. (2009) to our M_{200}, c_{200} convention, using the detailed relations found in Appendix C of Hu & Kravtsov (2003) or in the Appendix of Johnston et al. (2007). For the plotted M_{200} range, it turns out that $c_{200} \approx 0.83\ c_{\rm vir}$. From Fig. 13, we see that our best-fit value of $c_{200} = 5.4^{+1.4}_{-1.1}$ is most consistent with the nominal ΛCDM concentration value for lensing-selected clusters, and does not suggest the need for a concentration excess in this particular case. It's likely that larger strong lensing cluster samples will be needed to more robustly compare the distribution of concentration values with the predictions of ΛCDM models.

7. Source Galaxy Star Formation Rate

We can use the [OII]3727 line in the calibrated spectra described in § 3.3 to estimate the star formation rate (SFR). As noted by Kennicutt (1998) the luminosities of forbidden lines like [OII]3727 are not directly coupled to the ionizing luminosity and their excitation is also sensitive to abundance and the ionization state of the gas. However the excitation of [OII] is well behaved enough that it can be calibrated through Hα as an SFR tracer. This indirect calibration is very useful for studies of distant galaxies because [OII]3727 can be observed out to redshifts $z \approx 1.6$ and it has been measured in several large samples of faint galxies (see references in Kennicutt (1998)). If we know the [OII] luminosity then we can use equation 3 from Kennicutt (1998) to determine a star formation rate for the galaxy

$$\mathrm{SFR}(M_\odot\ \mathrm{yr}^{-1}) = (1.4 \pm 0.4) \times 10^{-41} (L[\mathrm{OII}])(\mathrm{ergs\ s}^{-1}) \tag{19}$$

where the uncertainty reflects the range between blue emission-line galaxies (lower limit) and more luminous spiral and irregular galaxies (upper limit).

As noted above, in order to extract the SFR we need to determine the total source flux from the [OII] line. We determine this using

$$f(\nu)_{[OII]} = \frac{f(\nu)_L}{f(\nu)_S} \times f(\nu)_I \tag{20}$$

where $f(\nu)_{[OII]}$ is the total flux emitted by the source in the [OII] line, $f(\nu)_L$ is the flux measured in the [OII] line in each spectrum, $f(\nu)_S$ is the flux in the knot spectrum contained within the i-band filter band pass and $f(\nu)_I$ is the flux from the source in the i-band.

Using the GALFIT-subtracted i-band image we determine $f(\nu)_I$ by summing the flux in an annulus of width $3''$ that encompasses the arcs. The flux $f(\nu)_L$ is measured by fitting a gaussian plus a continuum to the [OII] line in each spectrum and integrating the flux under the gaussian fit. The flux $f(\nu)_S$ is calculated as follows. For each spectrum we first fit the continuum level, we then add the fitted continuum plus the [OII] line flux and convolve it with the filter response curve for the SDSS i-band filter and integrate the convolved spectrum.

We have determined $f(\nu)_{[OII]}$ separately for each knot that was targeted for spectra. The fluxes are listed in Table 6 for each knot. We convert $f(\nu)_{[OII]}$ into an [OII] luminosity and then use Equation 19 to determine a star formation rate for each knot. This rate is the raw rate which must be scaled by the lens magnification f_{lens} to determine the true rate. We quote the SFR for the two values of f_{lens} that were determined in §4. We assume one magnitude of extinction (Kennicutt 1998) and have corrected the measured [OII] luminosity to account for this. This yields the star formation rates listed in Table 6 for the two values of f_{lens}. The rate for knot A3 is higher by a factor of 2 compared to the others because it has a small $f(\nu)_S$ compared to the other knots but the value of $f(\nu)_L$ is quite similar to the other knots. This can clearly be seen in Figure 6. We can combine the measurements for the four knots using a simple average to quote an overall SFR. This yields values of SFR($f_{lens} = 49$) $= 4.6 \pm 0.7$ and SFR($f_{lens} = 141$) $= 1.3 \pm 0.2$.

These rates are significantly smaller that those obtained for the 8 o'clock arc (Allam et al. 2007) and the Clone (Lin et al. 2009) which were $229 M_\odot$ yr^{-1} and $45 M_\odot$ yr^{-1} respectively (after converting to our chosen cosmology). Both these systems were at much higher redshift (2.72 and 2.0 respectively) so one would potentially expect higher rates from these systems. They also had smaller values of f_{lens}. We can compare our result to blue galaxies at similar redshift from the DEEP2 survey (Cooper et al. 2008). Using Figure 18 of Cooper et al. (2008) we obtain a median SFR of about $34 M_\odot$ yr^{-1} for a redshift $z = 0.9$ galaxy which is also higher than our measurement. Other measurements using the AEGIS field (Noeske et al. 2007) give a median SFR ranging from $10 M_\odot$ yr^{-1} to $40 M_\odot$ yr^{-1} depending weakly on the galaxy mass, which is unknown in our case. Our measurement can be compared to the far-right plot of Figure 1 in Noeske et al. (2007) and we fall on the low side of the measured data. Note that these conclusions are dependent on the magnification values used, for example smaller values such as those obtained for the Clone or the 8 o'clock arc would yield larger values for the SFR.

8. Conclusions

We have reported on the discovery of a star-forming galaxy at a redshift of $z = 0.9057$ that is being strongly lensed by a massive galaxy cluster at a redshift of $z = 0.3838$.

The Einstein radius determined from the lensing features is $\theta_{EIN} = 7.53 \pm 0.25''$ and the enclosed mass is $(1.5 \pm 0.1) \times 10^{13} M_{\odot}$, with a corresponding SIS velocity dispersion of $\sigma = 694 \pm 12$ km s^{-1}.

Using GMOS spectroscopic redshifts measured for 30 cluster member galaxies, we obtained a velocity dispersion $\sigma_c = 855^{+108}_{-96}$ km s^{-1} for the lensing cluster.

We have derived estimates of M_{200} from measurements of (1) weak lensing, (2) weak + strong lensing, (3) velocity dispersion σ_c, and (4) cluster richness $N_{200} = 55$. We obtained the following results for M_{200}: (1) M_{200}(weak lensing) $= 5.0^{+2.9}_{-2.3} \times 10^{14} M_{\odot}$, (2) M_{200}(lensing) $= 4.9^{+2.9}_{-2.2} \times 10^{14} M_{\odot}$, (3) $M_{200}(\sigma_c) = 5.79^{+2.22}_{-1.99} \times 10^{14} M_{\odot}$ (assuming no velocity bias, $b_v = 1$), and (4) $M_{200}(N_{200}) = (4.6 \pm 2.1) \times 10^{14} M_{\odot}$. These results are all very consistent with each other. The combination of the results from methods 2, 3 and 4 give $M_{200} = 5.1^{+1.3}_{-1.3} \times 10^{14} M_{\odot}$, which is fully consistent with the individual measurements but with an error that is smaller by a factor of nearly two. The final NFW concentration from the combined fit is $c_{200} = 5.4^{+1.4}_{-1.1}$, which is also consistent with the lensing-based value but again with a smaller error.

We have compared our measurements of M_{200} and c_{200} with predictions for (a) clusters from ΛCDM simulations, (b) lensing selected clusters from simulations, and (c) a real sample of cluster lenses from Oguri et al. (2009). We find that we are most compatible with the predictions from ΛCDM simulations for lensing clusters, and we see no evidence that an increased concentration is needed for this one system. We are studying this further using other lensing clusters we observed from the SDSS (Diehl et al. 2009). These clusters will be the subject of a future paper.

Finally, we have estimated the star forming rate (SFR) to be between 1.3 to 4.6 $M_{\odot}$ yr^{-1}, depending on magnification. These are small star-forming rates when compared to some of our previously reported systems, and are also small when compared with rates found for other galaxies at similar redshifts. However we caution that this conclusion is entirely dependent on the derived lens magnification.

We thank the anonymous reviewer for helpful comments which have improved the paper.

Based on observations obtained at the Gemini Observatory, which is operated by the Association of Universities for Research in Astronomy, Inc., under a cooperative agreement with the NSF on behalf of the Gemini partnership: the National Science Foundation (United States), the Science and Technology Facilities Council (United Kingdom), the National Research Council (Canada), CONICYT (Chile), the Australian Research Council (Australia), Ministério da Ciência e Tecnologia (Brazil) and Ministerio de Ciencia, Tecnología e Innovación Productiva (Argentina). Gemini Proposal ID GS-2007B-Q-228.

The Blanco Cosmology Survey was performed on the Blanco 4m telescope located at the Cerro Tololo Inter-American Observatory (National Optical Astronomy Observatory) which is operated by the Association of Universities for Research in Astronomy, under contract with the National Science Foundation.

S. S. Allam acknowledges support from an HST Grant. Support of program no. 11167 was provided by NASA through a grant from the Space Telescope Science Institute, which is operated by the Association of Universities for Research in Astronomy, Inc., under NASA contract NAS5-26555.

AZ and JM acknowledge the support of the Excellence Cluster Universe in Garching. Support for M.B. was provided by the W. M. Keck Foundation.

Thanks to Jeff Kubo for providing a copy of the Ellipto adaptive moments code. Thanks also go to Quarknet students Liana Nicklaus, Gina Castelvecchi, Braven Leung, Nick Gebbia, Alex Fitch, and their advisor Patrick Swanson, who worked with HL during summer 2009 on a weak lensing mass analysis of this cluster with different codes than used here.

Fermilab is operated by Fermi Research Alliance, LLC under Contract No. DE-AC02-07CH11359 with the United States Department of Energy.

REFERENCES

Allam, S., et al. 2007, ApJ, 662, 51

Auger, M.W., et al. 2010, ApJ, 724, 511

Bayliss, M.B., et al. 2010, preprint arXiv:1010.2714v2

Becker, M.R. et al. 2007 ApJ, 669, 905

Beers, T.C, Flynn, K., Gebhardt,K. 1990 ApJ, 100, 1

Bernstein, G.M., & Jarvis, M. 2002, AJ, 123, 583

Bertin, E., & Arnouts, S. 1996, A&AS, 117, 393

Bertin, E., et al., 2002, Astronomical Data Analysis Software and Systems XI, Astronomical Society of the Pacific Conference Series, Vol 281

Bertin, E., 2006, Astronomical Data Analysis Software and Systems XI, Astronomical Society of the Pacific Conference Series, Vol 351

Bolton, A., et al., 2008, ApJ, 682, 964

Bradač, M., et al., 2006, ApJ, 652,937

Bradač, M., et al., 2008a, ApJ, 681,187

Bradač, M., et al., 2008b, ApJ, 687,959

Broadhurst, T.J., & Barkana, R. 2008, MNRAS, 390, 1647

Bruzual, G., & Charlot, S. 2003, MNRAS, 344, 1000

Cabanac, R.A., et al., 2007, A&A, 461, 813

Chabrier, G. 2003, PASP, 115, 763

Clowe, D., & Schneider, P. 2001, A&A, 379, 384

Coleman, G.D., Wu, C.-C., & Weedman, D.W. 1980, ApJS, 43, 393

Cooper, M.C., et al., 2008, MNRAS, 383, 1058

Deb, S., et al., 2008, ApJ, 687, 39

Diego, J.M., et al., 2007, MNRAS, 375, 958

Diehl, H.T., et al 2009 ApJ, 707, 686

Duffy, A.R., et al. 2008, MNRAS, 390, L64

Evrard, E.A., et al. 2008, ApJ, 672, 122

Faure, C., et al., 2008, ApJS, 176, 19

Fukugita, M., et al., 1995, PASP, 107, 945

Hansen, S.M., et al., 2005, ApJ, 633, 122

Hennawi, J.F., et al., 2008, AJ, 135, 664

Hicks, A.K., at al., 2007, ApJ, 671,1446

Hirata, C.M., et al. 2004, MNRAS, 352, 529

Hirata, C., & Seljak, U. 2003, MNRAS, 343, 459

Hu, W., & Kravtsov, A.V. 2003, ApJ, 584, 702

Ilbert, O., et al. 2006, A&A, 457, 841

Jackson, N., et al. 2008, MNRAS, 389, 1311

Johnston, D.E., et al. 2007, preprint arXiv:0709.1159v1

Jouvel, S., et al. 2009, A&A, 504, 359

Kennicutt, R.C. 1998, ARA&A, 36, 189

King, L.J., & Schneider, P. 2001, A&A, 369, 1

Koester, B.P., et al. 2007a, ApJ, 660, 221

Koester, B.P., et al. 2007b, ApJ, 660, 239

Kubo, J.M., et al. 2007, ApJ, 671, 1466

Kubo, J.M., et al. 2009, ApJ, 702, L110

Kurtz, M.J., & Mink, D.J., 1998, PASP, 110, 934

Limousin, et al., 2007, ApJ, 668, 643

Lin, H., et al. 2007, Gemini Proposal GS-2007B-Q-228

Lin, H., et al. 2009, ApJ, 699, 1242

Mandelbaum, R., et al. 2008, MNRAS, 386, 781

Maughan, B.J., et al., 2004 MNRAS, 351, 1193

Merten, J., et al., 2009, A&A, 500, 681

Mohr J., et al., 2008, Observatory Operations: Strategies, Processes, and Systems II, Proceedings of the SPIE, Volume 7016, pp. 70160L-70160L-16

Narayan, R., & Bartelmann, M. 1996, preprint arXiv:astro-ph/9606001

Natarajan, P., et al., 1998, ApJ, 499, 600

Natarajan, P., et al., 2002, ApJ, 580, L11

Navarro, J.F., Frenk, C.S., & White, S.D.M. 1995, MNRAS, 275, 720

Ngeow, C., et al., 2006, Observatory Operations: Strategies, Processes, and Systems, Proceedings of the SPIE, Volume 6270, pp. 627023

Noeske, K.G., et al., 2007, ApJ, 660, L43

Oguri, M., & Blandford, R.D. 2009, MNRAS, 392, 930

Oguri, M., et al., 2009, ApJ, 699, 1038

Okabe, N., et al., 2010, PASJ, 62, 811

Peng, C., et al. 2002, AJ, 124, 266

Pointecouteau, E., et al., 2004, A&A, 423, 33

Read, J., http://www.itp.uzh.ch/ justin/Astro/Lectures/PixeLens/tutorial.pdf

Richard, J., et al. 2010, MNRAS, 404, 325

Rozo, E., et al., 2009, ApJ, 699, 768

Rozo, E., et al., 2010, ApJ, 708, 645

Saha, P., & Williams, L.L.R, 2004 AJ, 127, 2604

Saha, P., & Williams, L.L.R, 2006 AJ, 653, 936

Smith, D.R., et al. 2001, ApJ, 551, 643

Vanderlinde. K., et al. 2010 ApJ, 722, 1180

Willis, J.P., et al., 2006, MNRAS, 369, 1521

Wright, C.O., & Brainerd, T.G. 1999, ApJ, 534, 34

Zenteno, A., et al., 2011 ApJ, 734, 3

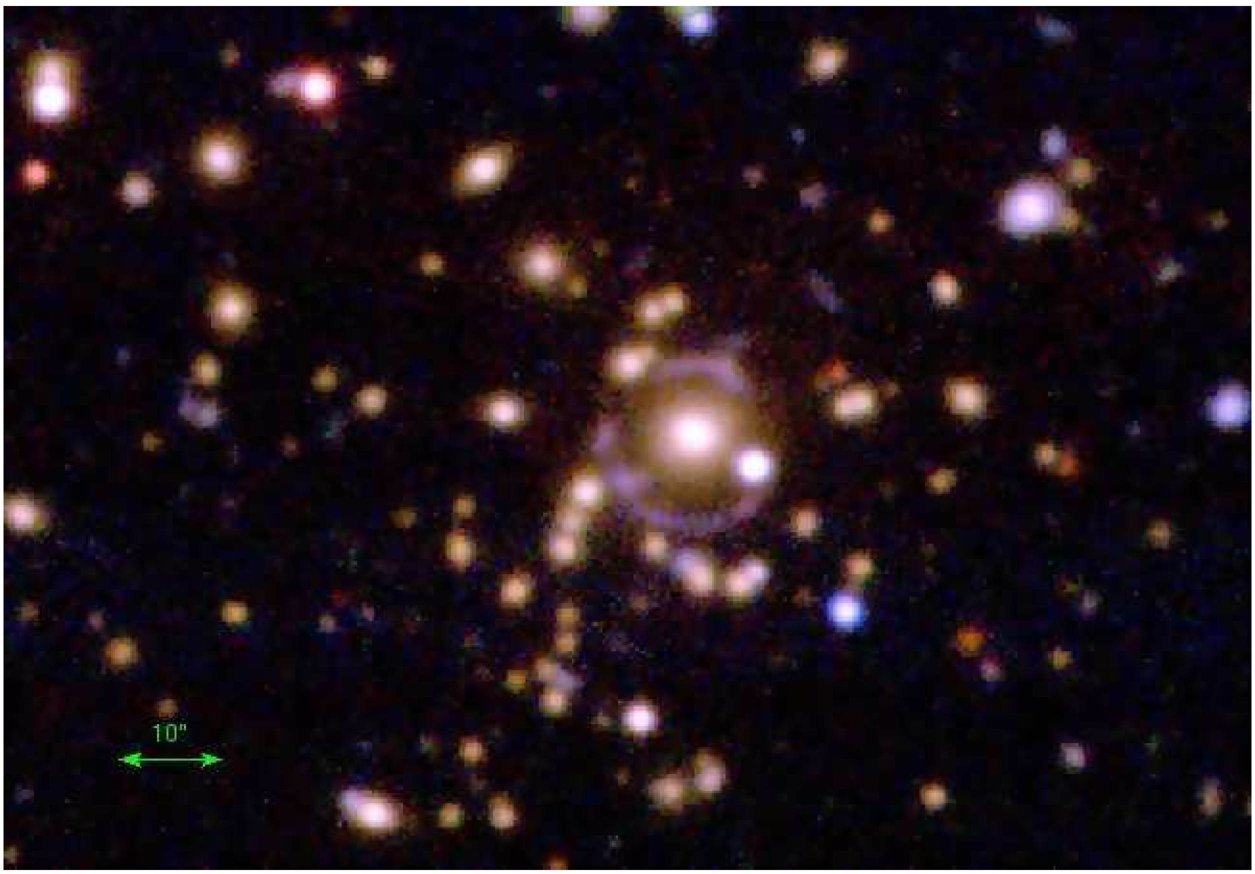

Fig. 1.— A *gri* color image of the Elliot Arc and its cluster environment. The scale is indicated by the horizontal arrow.

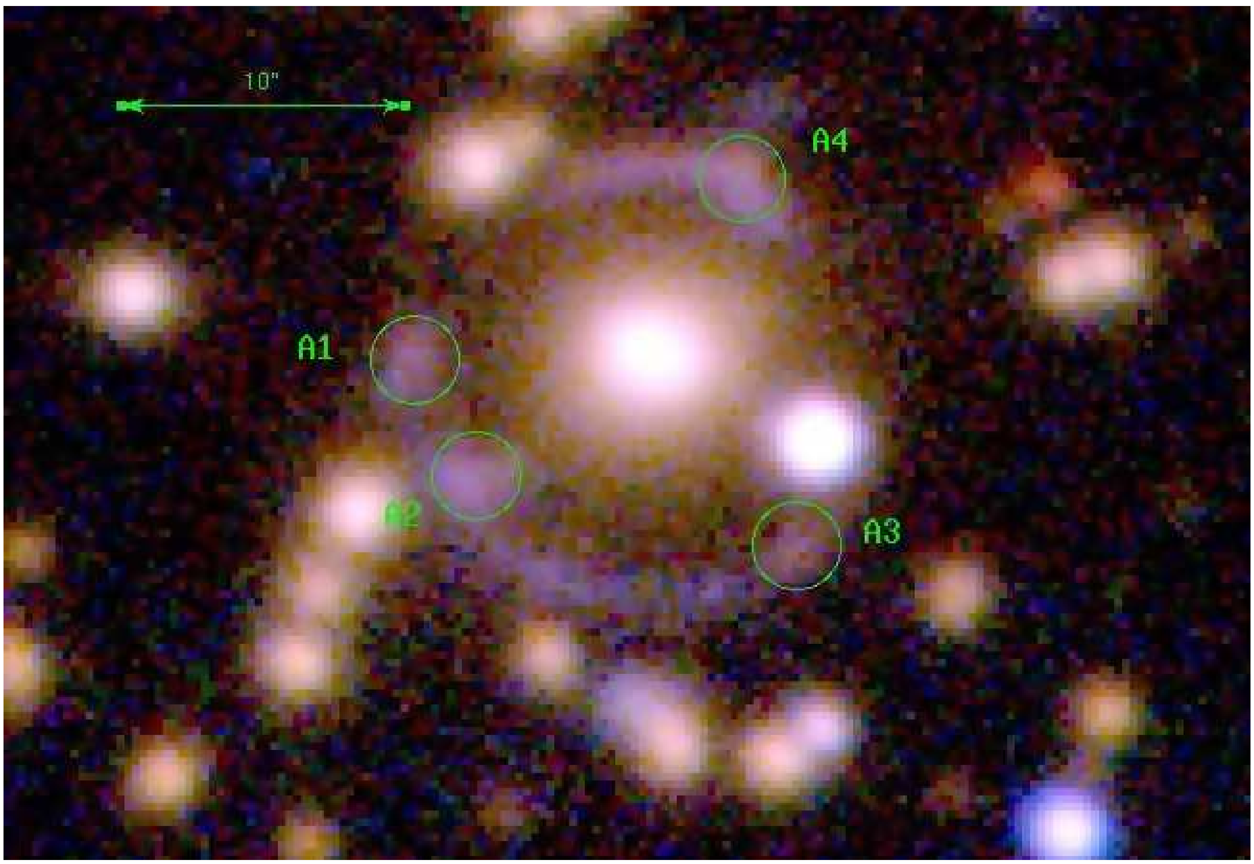

Fig. 2.— A *gri* color image of the Elliot Arc. The knots targeted for spectroscopy are shown as green circles. The scale is indicated by the horizontal line.

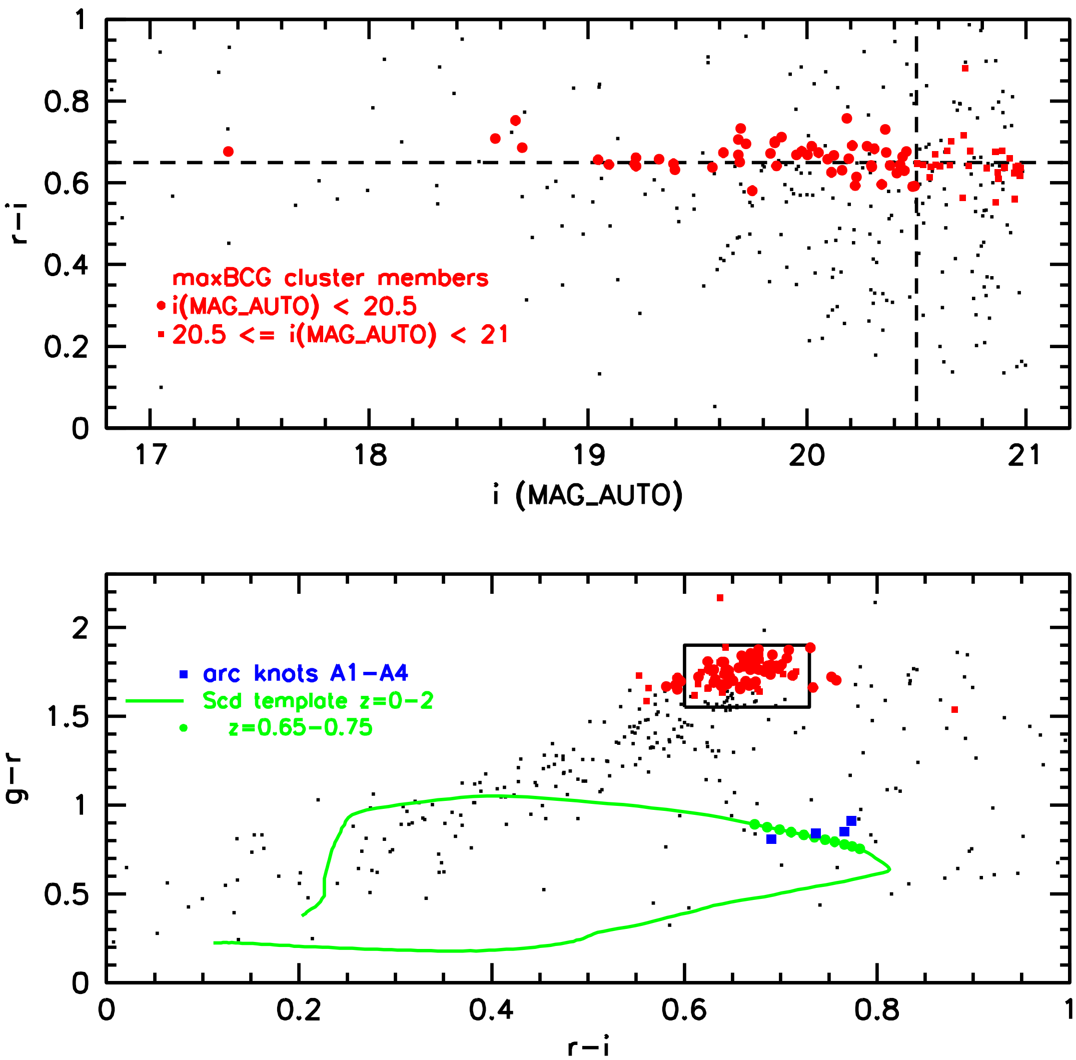

Fig. 3.— (Top) $r - i$ vs. i(MAG_AUTO) color-magnitude diagram for all galaxies (black points) with $i < 21$ and within a radius $r_{200}^{gal} = 1.51\ h^{-1}$ Mpc ($= 6.88'$) of the BCG. Colors are measured using $3''$-diameter aperture magnitudes. Galaxies meeting the maxBCG cluster color selection criteria (see §3.2) are plotted in red, with red circles indicating cluster members brighter than $i = 20.5$, and red squares indicating fainter cluster members. (Bottom) $g-r$ vs. $r - i$ color-color diagram for the same galaxies as in the top panel. Red circles and squares again indicate brighter and fainter maxBCG cluster members, while the black rectangle indicates the color selection box (approximating the more detailed maxBCG color criteria) used to select likely cluster galaxies for GMOS spectroscopy (see §3). In addition, the 4 bright knots A1-A4 (Fig. 2) in the lensed arcs are shown by the blue squares. The green curve is an Scd galaxy model (Coleman, Wu, & Weedman 1980) at redshifts $z = 0 - 2$, with green circles highlighting the redshift range $z = 0.65 - 0.75$, indicating an approximate photometric redshift $z \sim 0.7$ for the arc knots.

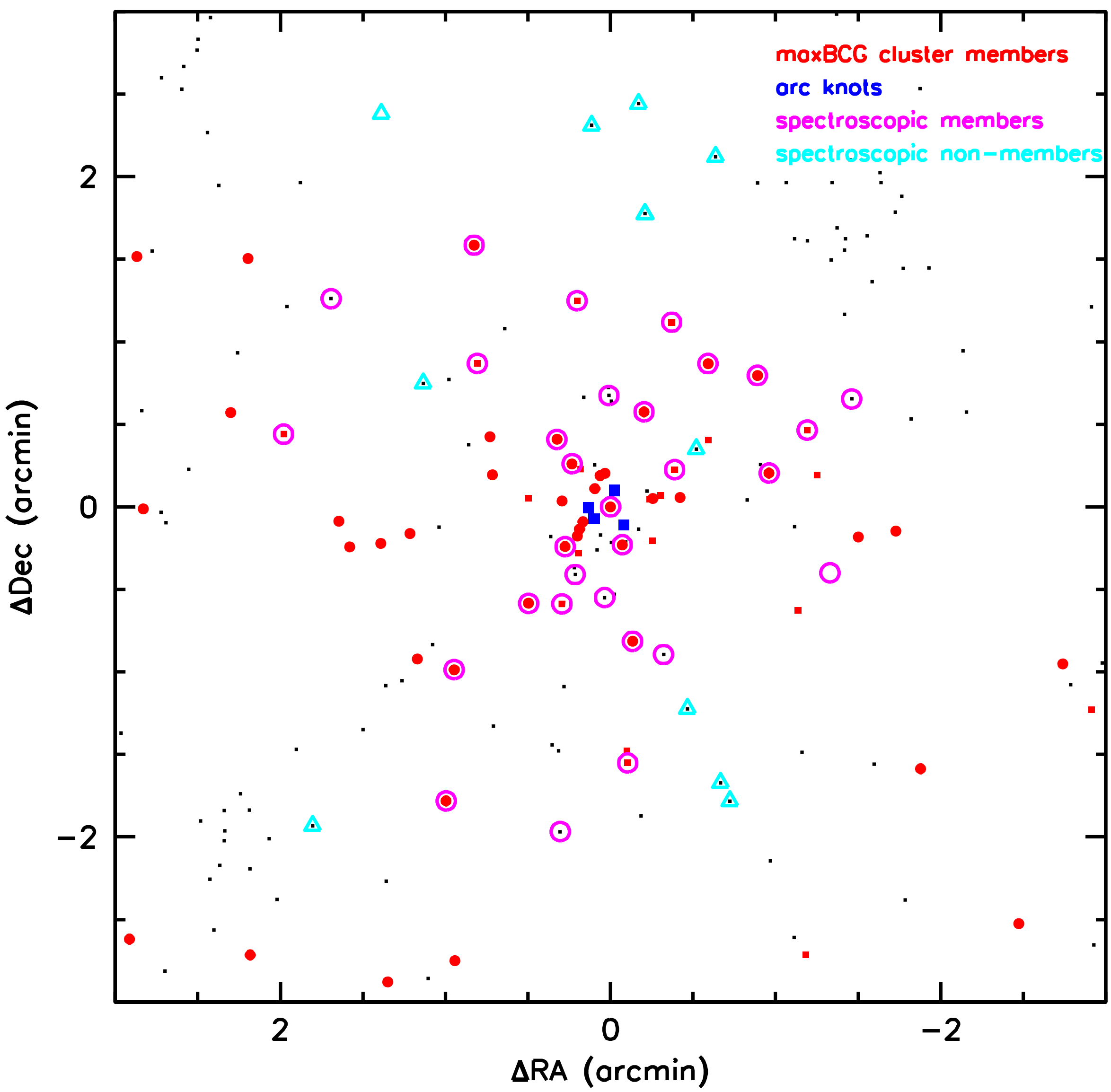

Fig. 4.— Relative positions of all galaxies (points) with i(MAG_AUTO) < 21 within a $6' \times 6'$ box centered on the BCG. Cluster member galaxies defined using maxBCG criteria (see §3.2) are plotted in red, with red circles indicating members brighter than $i = 20.5$, and red squares indicating fainter members. The 4 bright knots A1-A4 (Fig. 2) in the lensed arcs are shown by the blue squares. Galaxies determined to be cluster members from GMOS redshifts are plotted with open magenta circles, while those found spectroscopically to be non-members are shown with open cyan triangles (see §3.3). North is up and East is to the left.

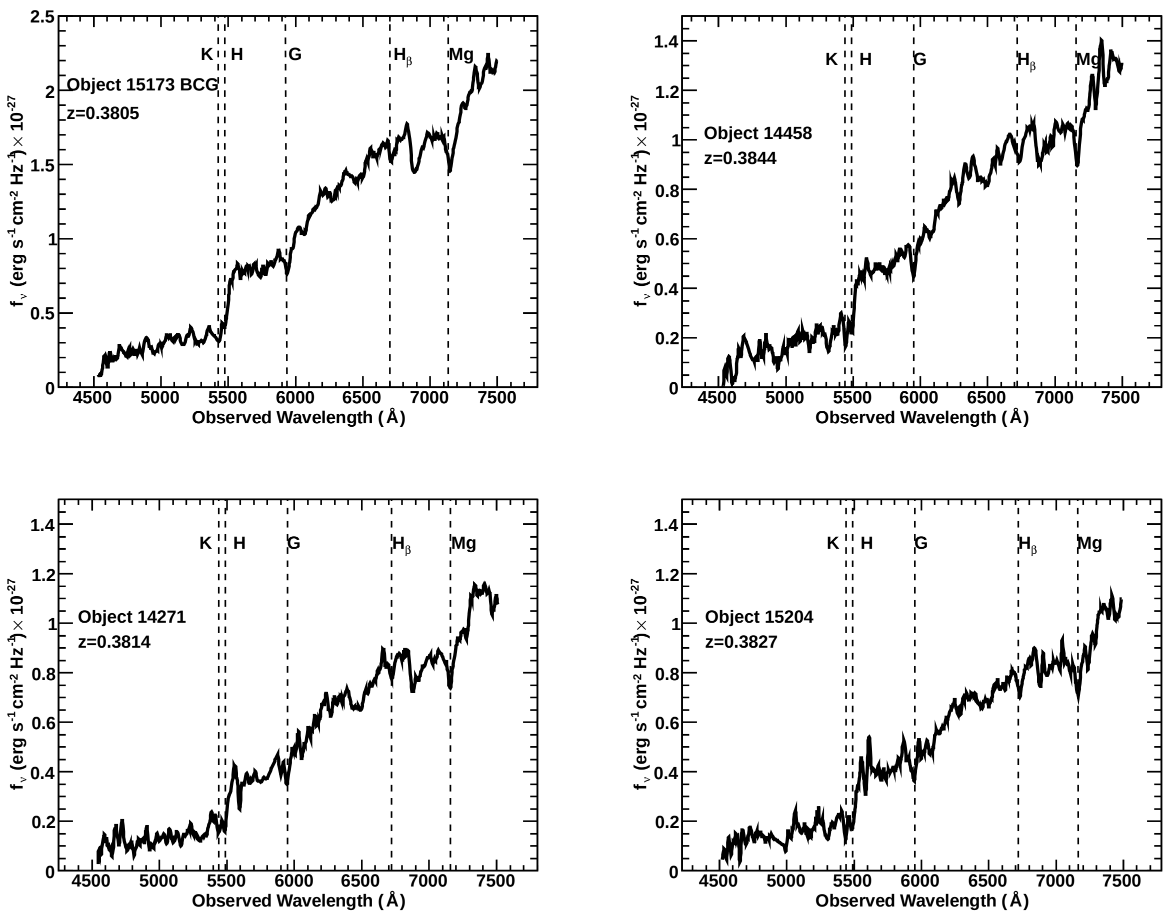

Fig. 5.— Four examples of flux-calibrated cluster member spectra (in f_ν). The spectra have been smoothed (with a boxcar of 5 pixels = 17.8 Å) to improve the signal-to-noise ratio. The spectrum in the top left is that of the BCG. The prominent absorption features used in the redshift identification are marked.

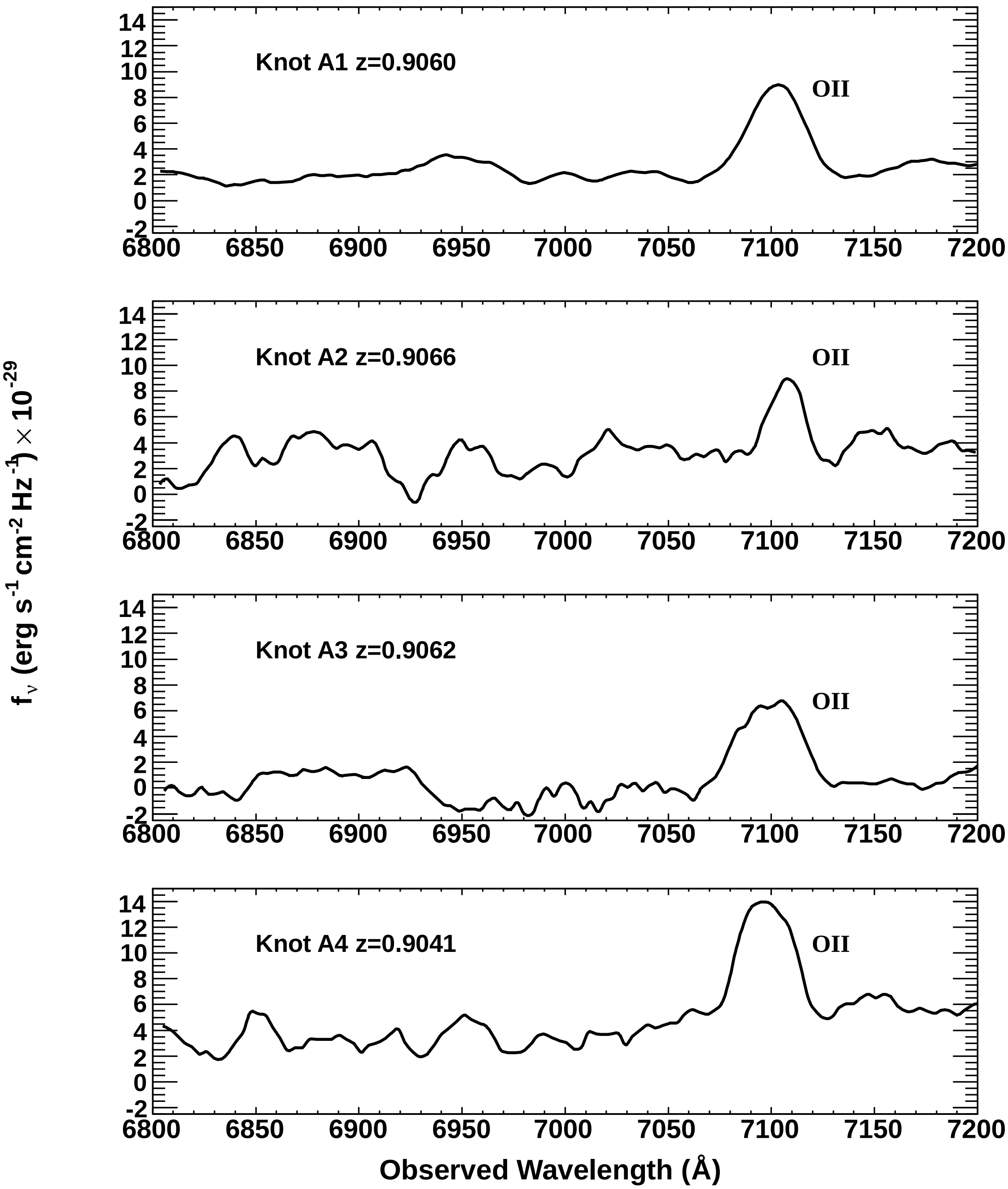

Fig. 6.— Flux-calibrated spectra (in f_ν) for the knots A1-A4. The spectra have been smoothed (with a boxcar of 5 pixels = 17.8Å) to improve S/N. Knot A2 was observed under seeing conditions that were a factor of two worse than for the other three knots. The [O II] 3727 Å line is marked.

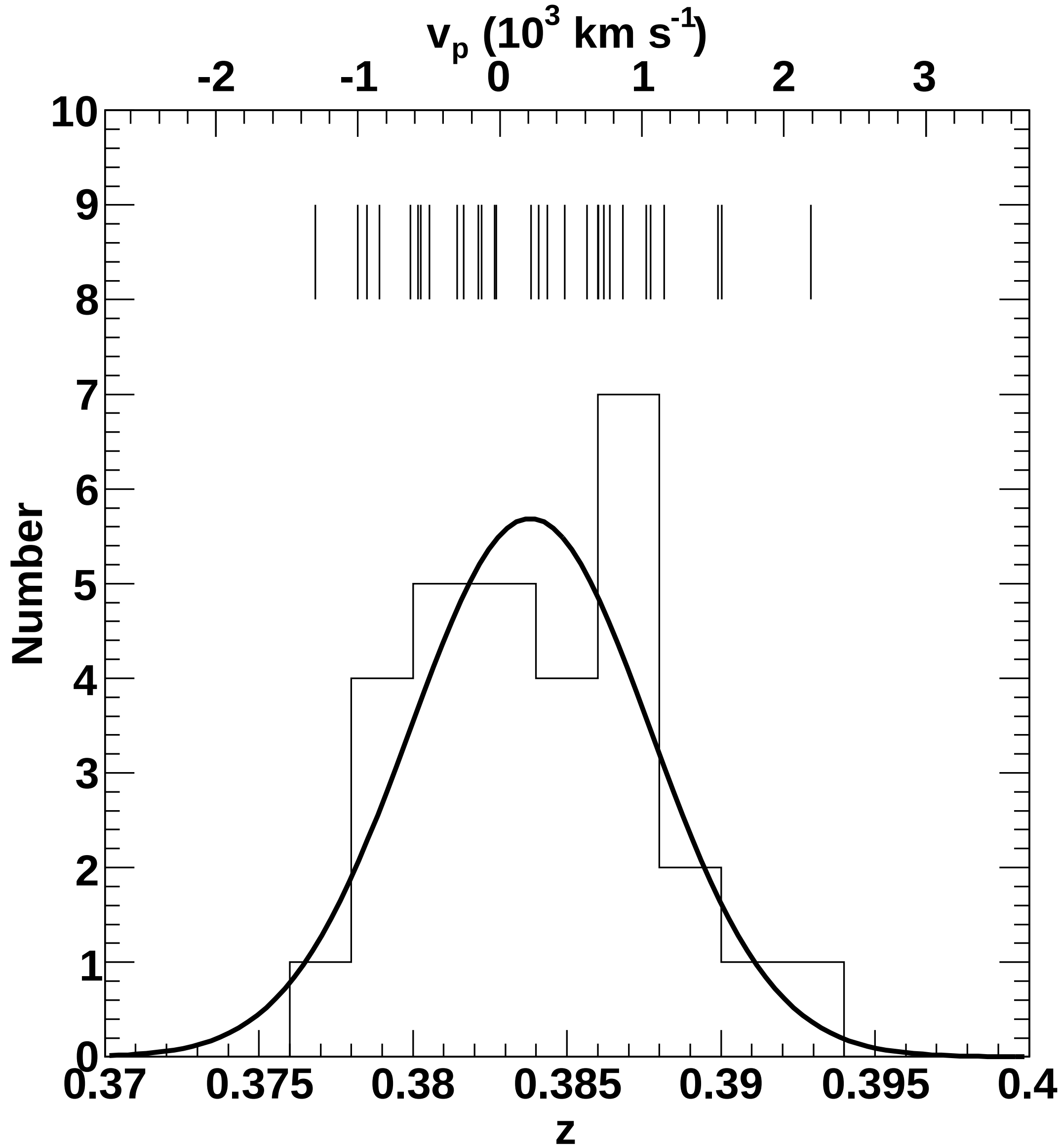

Fig. 7.— The redshift distribution for the 30 cluster members in Table 3. The tick marks at the top represent the individual cluster member peculiar velocities. The solid line is a Gaussian with mean and sigma equal to z_c and $\sigma_c \times (1 + z_c)$ respectively (see §3.4).

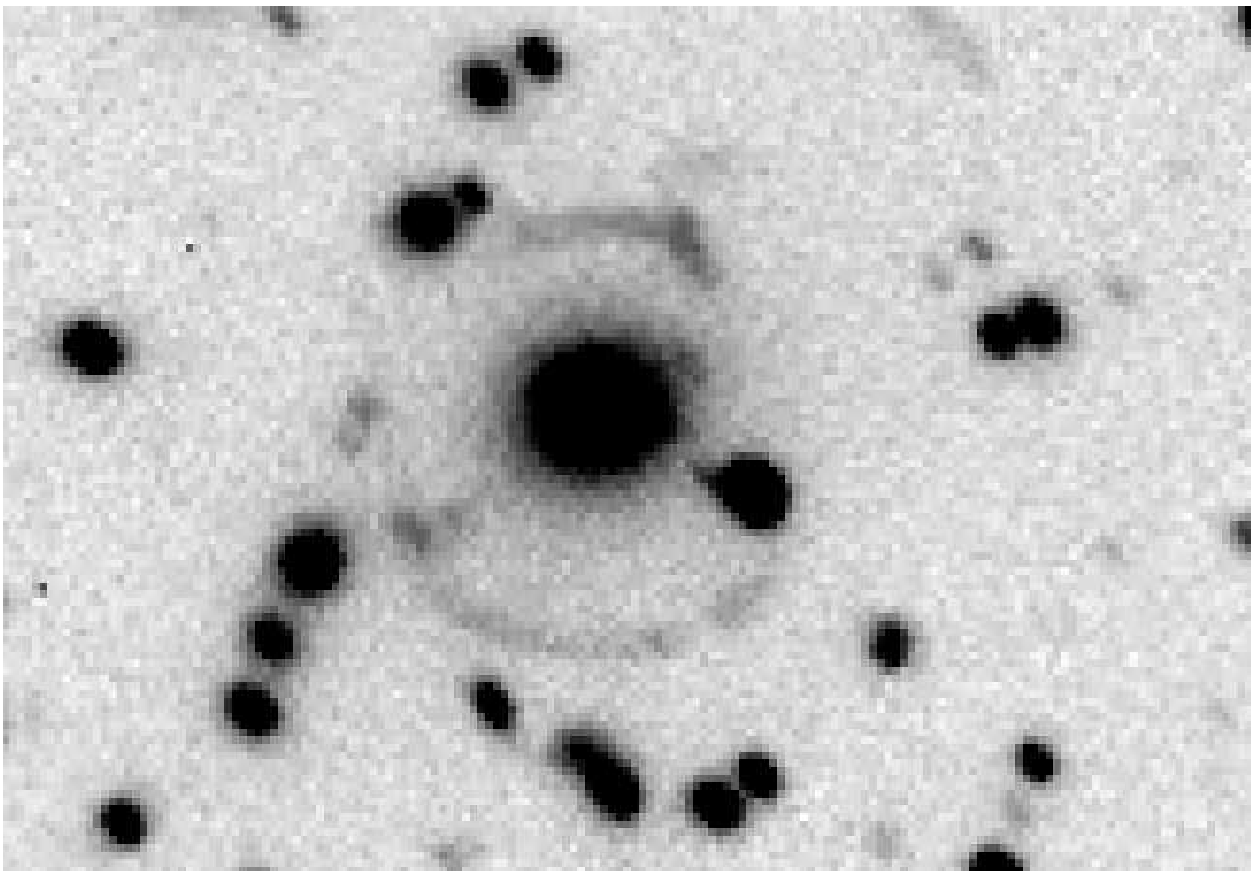

Fig. 8.— The coadded r-band image. The lensing features can be clearly seen.

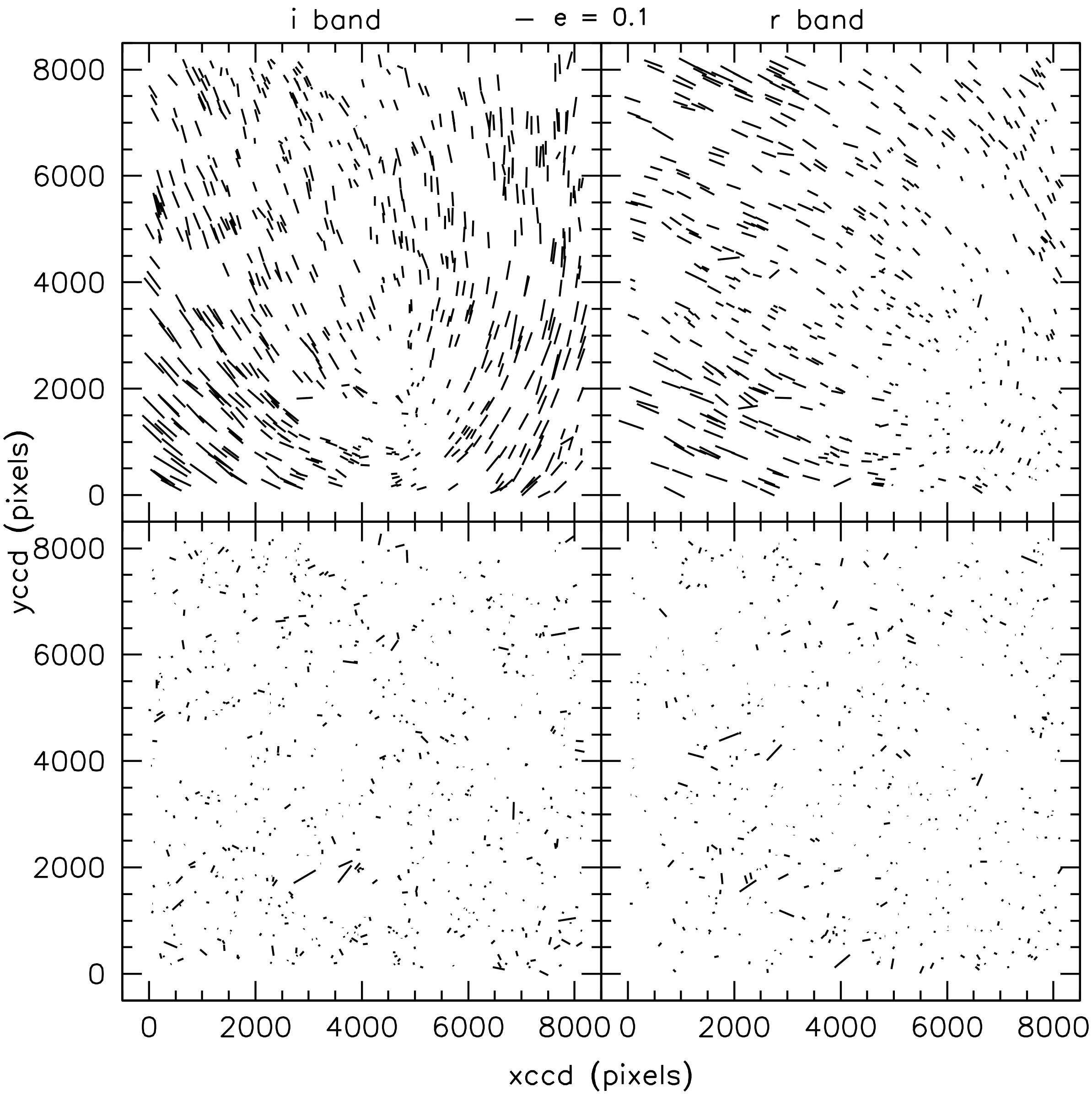

Fig. 9.— (*Top panels*) "Whisker" plots that show the clear spatial variation of the PSF ellipticity vs. CCD x, y position in our i- (*left*) and r-band (*right*) images. The size of each whisker is proportional to the PSF ellipticity $e_{PSF} = \sqrt{e_{1,PSF}^2 + e_{2,PSF}^2}$, where a whisker with ellipticity $e = 0.1$ is shown at the top center of the figure. Each whisker is oriented at an angle $\theta_{PSF} = \frac{1}{2}\tan^{-1}(e_{2,PSF}/e_{1,PSF})$ counterclockwise from horizontal. (*Bottom panels*) The corresponding whisker plots after subtraction of the PSF model described in §5.2, showing the removal of the bulk of the spatial variation of the PSF ellipticities.

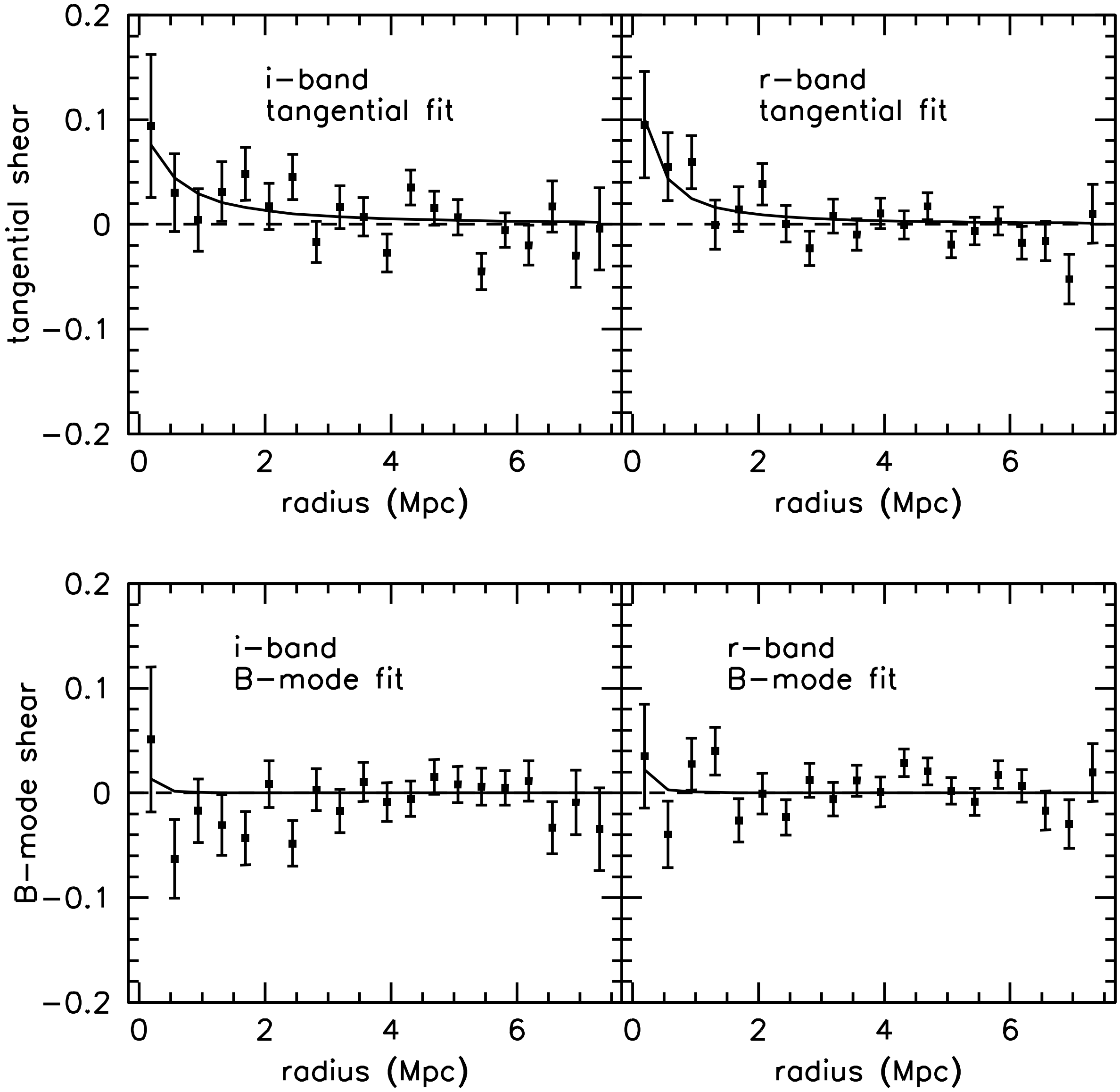

Fig. 10.— The points with error bars show the tangential (top) and B-mode (bottom) radial shear profiles for the galaxy sample used for weak lensing analysis in the i (left) and r (right) filters. In each panel, the solid curve shows the shear profile for the best-fitting NFW mass density profile, as determined via the procedure described in §5.3. The dashed horizontal lines indicate zero shear. The best-fit NFW parameters and details of the galaxy sample are given in Table 5.

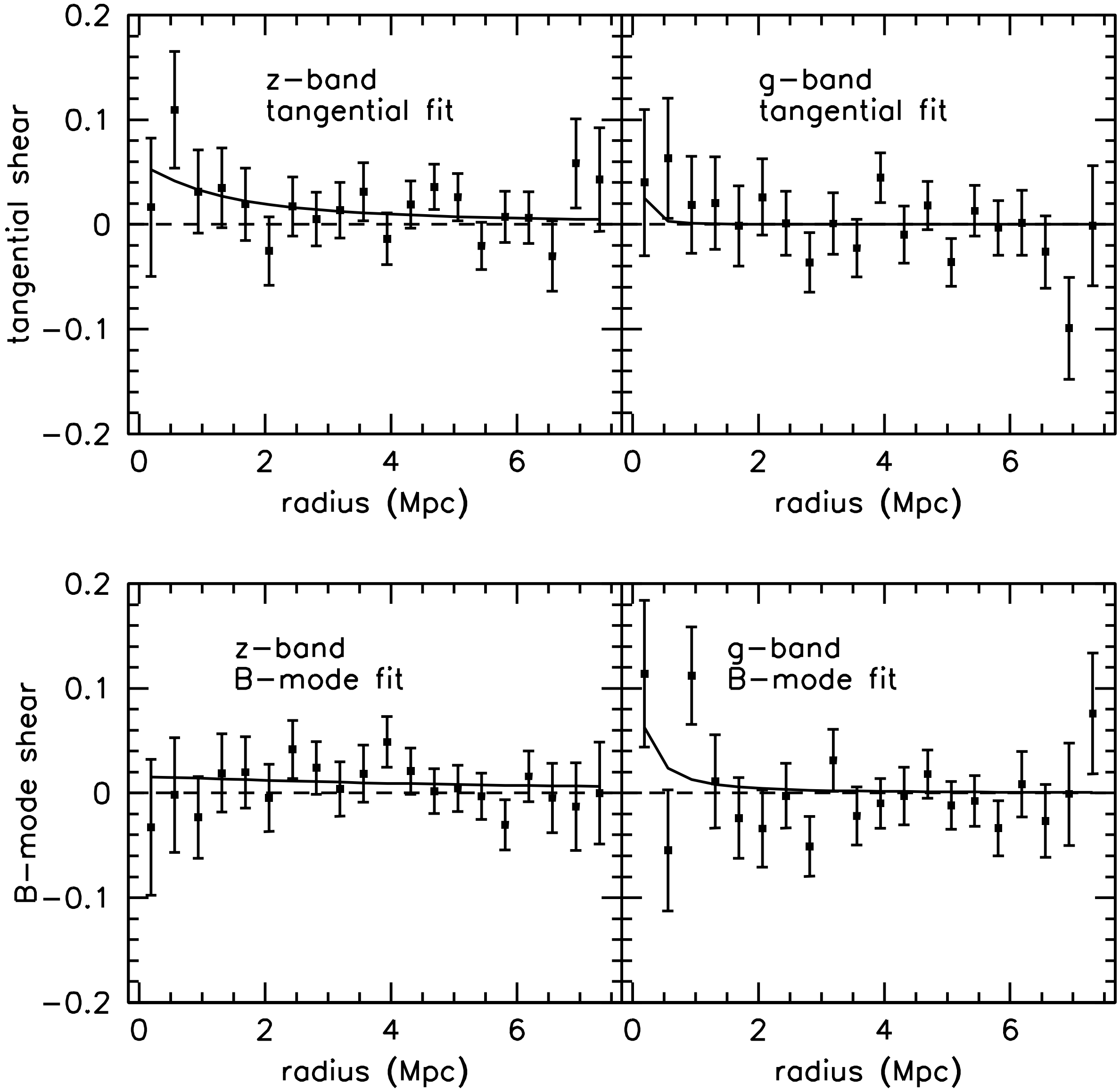

Fig. 11.— Similar to Figure 10, but for the z (left) and g (right) filters.

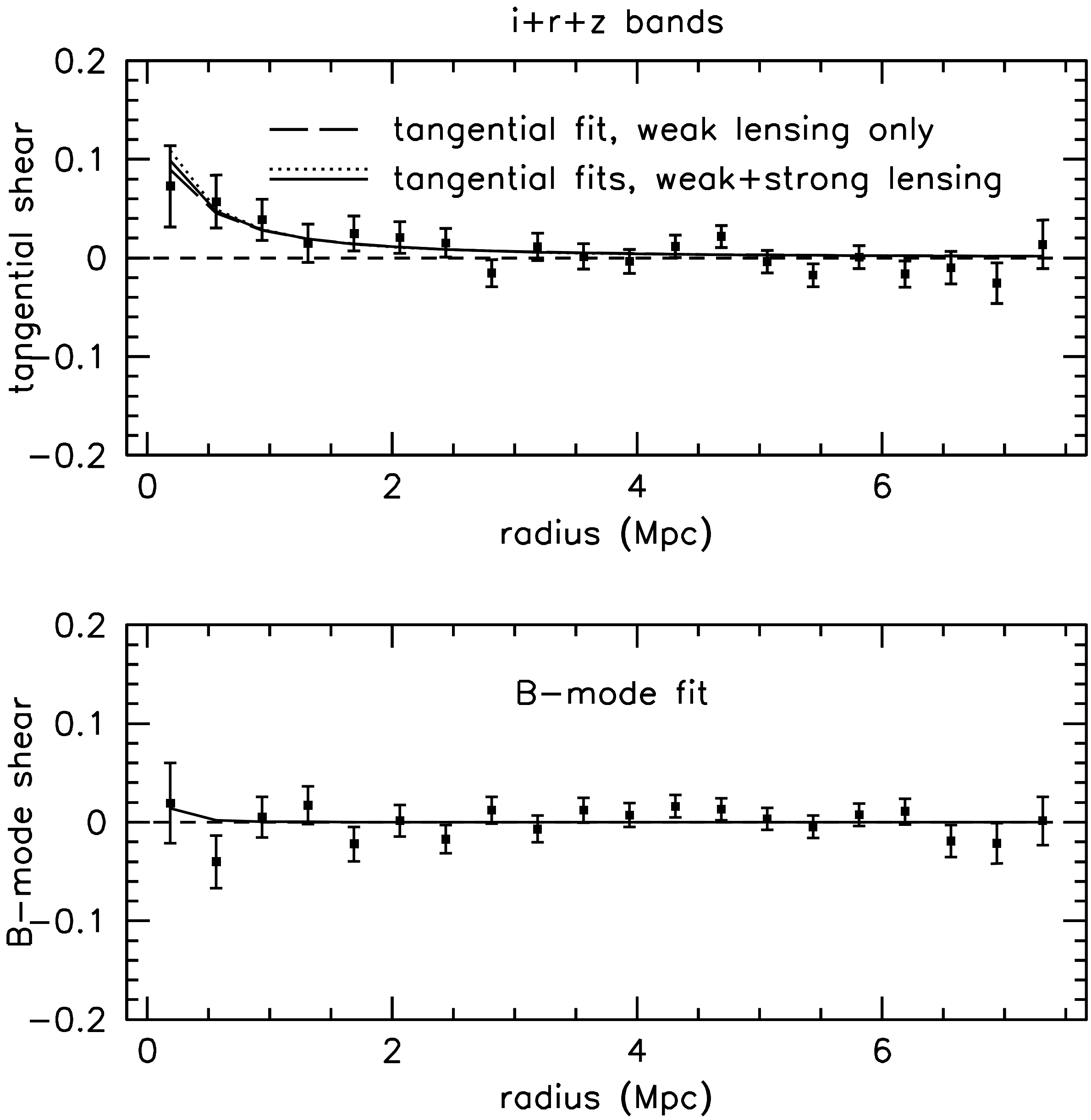

Fig. 12.— Similar to Figure 10, but for the multi-filter $i + r + z$ sample. For the tangential shear profile fits in the top panel, the long-dashed curve gives the results using weak lensing only, while the dotted and solid curves give the results using combined weak plus strong lensing. The dotted curve is for the case where we estimated the dark matter mass within the Einstein radius by subtracting off just a stellar mass contribution, while the solid curve is for the case where we also subtracted off an estimated gas mass contribution. See §5.4, §6.1, and Table 5 for details.

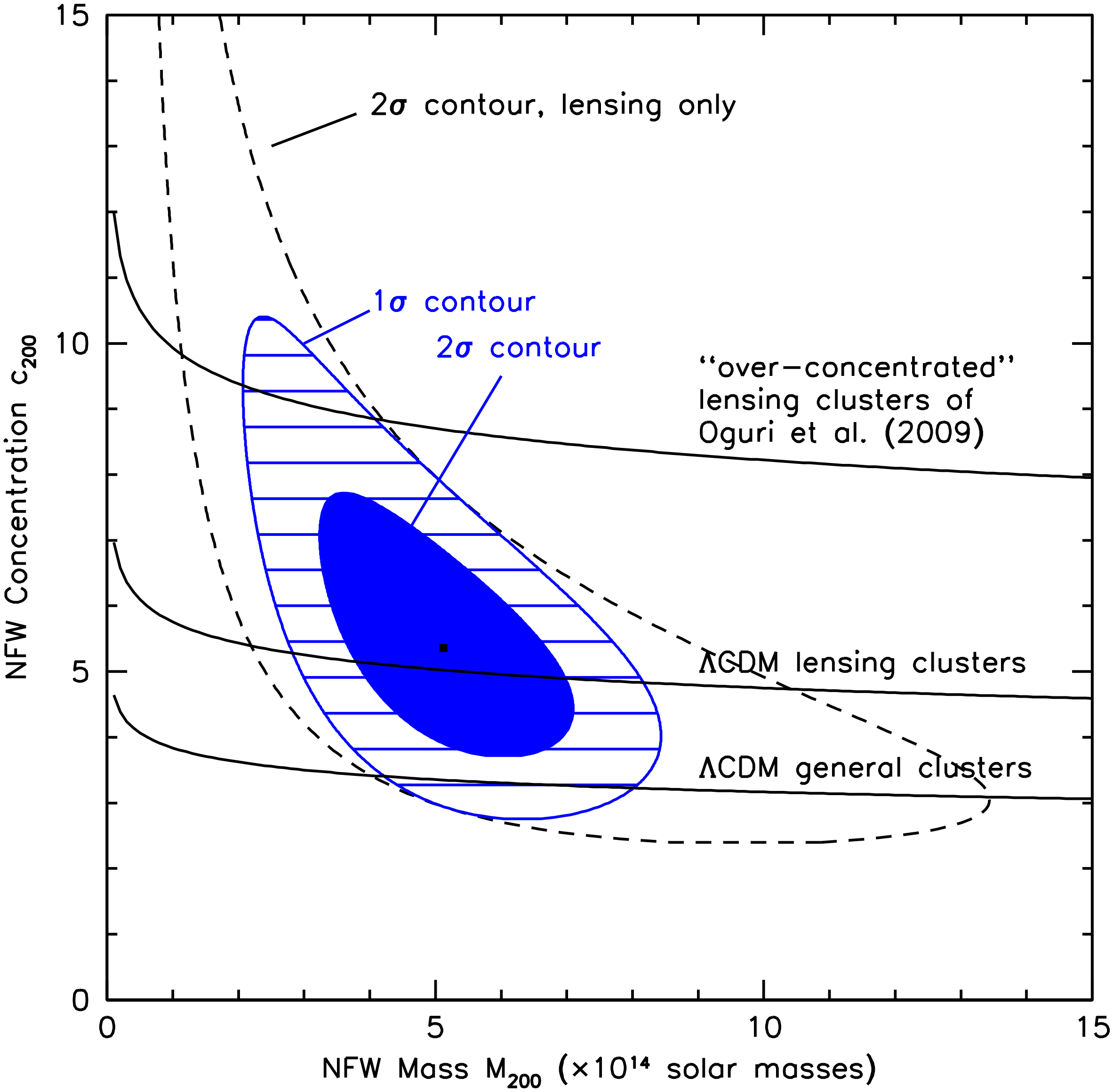

Fig. 13.— Confidence contours for the best-fitting NFW mass M_{200} and concentration c_{200}, obtained by combining the lensing, velocity dispersion, and cluster richness constraints, as described in §6.2. The 2-parameter, 1σ contours are shown in solid blue, while the 2σ contours are shown in hatched blue. The outer dashed contours show the 2-parameter, 2σ constraints derived solely from the weak + strong lensing analysis of §6.1. Also, as described in §6.2, the 3 mostly horizontal curves show the concentration vs. mass relation at $z = 0.4$ for: (bottom) clusters overall from ΛCDM simulations; (middle) lensing selected clusters from simulations; and (top) a real lensing cluster sample from Oguri et al. (2009).

Table 1. Observation Log

Filter/Grating	UT Date	Exposure	Seeing	Notes
BCS Imaging				
g	14 Dec 2006	2×125 sec	1.44″	
r	14 Dec 2006	2×300 sec	1.29″	
g	11 Nov 2008	2×125 sec	1.03″	
r	11 Nov 2008	2×300 sec	0.88″	
i	30 Oct 2006	3×450 sec	1.18″	
z	30 Oct 2006	3×450 sec	1.31″	
GMOS spectroscopy				
GG455	4 Aug 2007	4×900 sec	0.56″	Mask 1 includes knots A1,A3,A4
GG455	4 Aug 2007	4×900 sec	1.14″	Mask 2 includes BCG and knot A2
GG455	4 Aug 2007	1×5 sec	-	Cu-Ar Mask 1
GG455	4 Aug 2007	1×5 sec	-	Cu-Ar Mask 2
GG455	14 Aug 2007	1×5 sec	-	1.5″ slit
GG455	14 Aug 2007	1×90sec	0.95″	Standard star EG21

Table 2. Knots Targeted for Spectroscopy

Knot	RA[a]	Dec[a]	$i(3'')$[b]	$g-r$[c]	$r-i$[c]
A1	357.912477	-54.881691	21.94	0.85	0.77
A2	357.911467	-54.882801	21.49	0.81	0.69
A3	357.906225	-54.883464	22.30	0.84	0.74
A4	357.907100	-54.879967	21.46	0.91	0.77

[a]RA and Dec are epoch J2000.0 and are given in degrees.

[b]i-band magnitudes for the knots are computed in $3''$-diameter apertures, after first subtracting a model of the BCG light derived using the Galfit galaxy fitting program (Peng et al. 2002).

[c]$g-r$ and $r-i$ colors are computed from $3''$-diameter SExtractor aperture magnitudes.

Table 3. Cluster Galaxies

Object ID[a]	RA[b]	Dec[b]	i(MAG_AUTO)[a]	$g-r$[a]	$r-i$[a]	redshift z[c]
maxBCG Cluster Members[d]						
15173 (BCG)	357.908555	-54.881611	17.36 ± 0.00	1.86 ± 0.01	0.68 ± 0.00	0.3805 ± 0.0003
16097	357.972190	-54.856522	18.58 ± 0.00	1.87 ± 0.02	0.71 ± 0.01	
16926	358.069064	-54.838013	18.67 ± 0.01	1.72 ± 0.02	0.75 ± 0.01	
14954	357.990606	-54.881805	18.70 ± 0.01	1.78 ± 0.02	0.69 ± 0.01	
14458	357.922935	-54.891348	19.05 ± 0.00	1.77 ± 0.02	0.66 ± 0.01	0.3844 ± 0.0002
15111	357.911305	-54.879770	19.10 ± 0.01	1.76 ± 0.03	0.64 ± 0.01	
13772	357.854114	-54.908062	19.21 ± 0.01	1.76 ± 0.02	0.65 ± 0.01	
14873	357.913389	-54.883120	19.22 ± 0.01	1.78 ± 0.02	0.66 ± 0.01	
15204	357.917968	-54.874795	19.22 ± 0.01	1.81 ± 0.02	0.64 ± 0.01	0.3827 ± 0.0002
15305	357.929749	-54.874524	19.32 ± 0.01	1.66 ± 0.02	0.66 ± 0.01	
15124	357.915316	-54.877257	19.39 ± 0.01	1.72 ± 0.03	0.65 ± 0.01	0.3929 ± 0.0005
11813	357.856326	-54.957697	19.40 ± 0.01	1.70 ± 0.03	0.63 ± 0.01	
13629	357.781583	-54.911494	19.57 ± 0.01	1.67 ± 0.03	0.64 ± 0.01	
16084	357.932492	-54.855191	19.62 ± 0.01	1.81 ± 0.03	0.67 ± 0.01	0.3864 ± 0.0003
14828	357.858498	-54.884039	19.69 ± 0.01	1.76 ± 0.03	0.67 ± 0.01	
15056	357.929263	-54.878393	19.69 ± 0.01	1.83 ± 0.03	0.71 ± 0.01	
13028	357.836914	-54.923702	19.69 ± 0.01	1.70 ± 0.03	0.65 ± 0.01	
14267	357.742239	-54.897565	19.70 ± 0.01	1.66 ± 0.04	0.73 ± 0.01	
13939	357.743518	-54.903441	19.72 ± 0.01	1.78 ± 0.04	0.70 ± 0.01	
14892	357.917045	-54.881040	19.75 ± 0.01	1.67 ± 0.03	0.58 ± 0.01	
17276	358.061857	-54.827190	19.83 ± 0.01	1.68 ± 0.03	0.67 ± 0.01	
12997	357.992988	-54.925261	19.85 ± 0.01	1.79 ± 0.04	0.70 ± 0.01	
14685	357.948912	-54.885316	19.85 ± 0.01	1.77 ± 0.03	0.70 ± 0.01	
14727	357.914364	-54.884540	19.86 ± 0.01	1.74 ± 0.04	0.64 ± 0.01	
12907	357.971817	-54.926860	19.88 ± 0.01	1.73 ± 0.03	0.71 ± 0.01	
15525	357.891439	-54.867148	19.95 ± 0.01	1.85 ± 0.04	0.67 ± 0.01	0.3802 ± 0.0005
13874	357.767222	-54.904760	19.98 ± 0.01	1.76 ± 0.04	0.68 ± 0.01	
14875	357.896375	-54.880676	20.00 ± 0.01	1.81 ± 0.04	0.67 ± 0.01	
14827	357.956282	-54.883059	20.02 ± 0.01	1.73 ± 0.04	0.69 ± 0.01	
14169	357.942454	-54.896963	20.05 ± 0.01	1.69 ± 0.04	0.67 ± 0.01	
14620	357.906482	-54.885446	20.09 ± 0.01	1.65 ± 0.03	0.66 ± 0.01	0.3822 ± 0.0004
11254	357.792343	-54.968633	20.11 ± 0.01	1.76 ± 0.03	0.63 ± 0.01	
19279	357.988291	-54.784591	20.12 ± 0.01	1.67 ± 0.04	0.67 ± 0.01	
15027	357.880749	-54.878200	20.16 ± 0.01	1.76 ± 0.04	0.63 ± 0.01	0.3876 ± 0.0006
12805	357.947638	-54.929596	20.18 ± 0.01	1.70 ± 0.04	0.76 ± 0.01	
13899	358.003818	-54.902294	20.19 ± 0.01	1.84 ± 0.04	0.66 ± 0.01	
14741	357.943783	-54.884299	20.21 ± 0.01	1.85 ± 0.05	0.69 ± 0.01	
12671	358.055413	-54.931583	20.22 ± 0.01	1.71 ± 0.04	0.59 ± 0.01	
14843	357.901141	-54.880772	20.23 ± 0.01	1.72 ± 0.04	0.61 ± 0.01	
14088	357.936003	-54.898050	20.27 ± 0.01	1.79 ± 0.05	0.69 ± 0.01	0.3816 ± 0.0005
14969	357.910388	-54.878452	20.29 ± 0.01	1.76 ± 0.05	0.64 ± 0.01	
12875	357.935888	-54.927451	20.30 ± 0.01	1.80 ± 0.04	0.64 ± 0.01	
13537	357.937414	-54.911304	20.31 ± 0.01	1.75 ± 0.04	0.68 ± 0.01	0.3849 ± 0.0003
15314	357.902668	-54.872019	20.34 ± 0.01	1.70 ± 0.05	0.60 ± 0.01	0.3841 ± 0.0004
14669	357.916522	-54.885626	20.36 ± 0.01	1.89 ± 0.06	0.73 ± 0.02	0.3862 ± 0.0003

Table 3—Continued

Object ID[a]	RA[b]	Dec[b]	i(MAG_AUTO)[a]	$g-r$[a]	$r-i$[a]	redshift z[c]
14639	357.954384	-54.885672	20.36 ± 0.01	1.77 ± 0.05	0.67 ± 0.01	
14232	357.904683	-54.895183	20.38 ± 0.01	1.76 ± 0.04	0.64 ± 0.01	0.3882 ± 0.0003
14703	357.865075	-54.884639	20.41 ± 0.01	1.81 ± 0.05	0.62 ± 0.02	
14690	357.914016	-54.883857	20.42 ± 0.01	1.68 ± 0.04	0.64 ± 0.01	
15463	357.882797	-54.868348	20.43 ± 0.01	1.71 ± 0.05	0.63 ± 0.01	0.3877 ± 0.0004
16005	357.991736	-54.856356	20.44 ± 0.01	1.70 ± 0.05	0.66 ± 0.01	
15333	357.975175	-54.872090	20.44 ± 0.01	1.69 ± 0.05	0.63 ± 0.01	
14972	357.909534	-54.878210	20.45 ± 0.01	1.87 ± 0.06	0.68 ± 0.02	
14086	357.829155	-54.897455	20.48 ± 0.01	1.68 ± 0.04	0.59 ± 0.01	
18418	357.768333	-54.801860	20.49 ± 0.01	1.65 ± 0.04	0.59 ± 0.01	
13764	357.905657	-54.906287	20.50 ± 0.01	1.73 ± 0.05	0.65 ± 0.01	
10692	357.819108	-54.981725	20.53 ± 0.02	1.71 ± 0.06	0.64 ± 0.02	
15516	357.931958	-54.867137	20.56 ± 0.01	1.68 ± 0.05	0.61 ± 0.01	0.3785 ± 0.0001
19588	357.961069	-54.776725	20.57 ± 0.02	1.64 ± 0.05	0.64 ± 0.02	
15002	357.897311	-54.877856	20.58 ± 0.01	1.70 ± 0.05	0.67 ± 0.02	0.3838 ± 0.0004
14800	357.901708	-54.880859	20.59 ± 0.01	1.73 ± 0.05	0.64 ± 0.01	
15788	357.914426	-54.860804	20.61 ± 0.01	1.75 ± 0.05	0.64 ± 0.02	0.3821 ± 0.0002
15373	357.965957	-54.874282	20.61 ± 0.01	1.66 ± 0.05	0.64 ± 0.02	0.3856 ± 0.0005
13697	357.905543	-54.907479	20.64 ± 0.01	1.81 ± 0.06	0.68 ± 0.02	0.3782 ± 0.0005
15187	357.874035	-54.873868	20.65 ± 0.01	1.89 ± 0.06	0.64 ± 0.02	0.3868 ± 0.0006
18026	358.056024	-54.810258	20.66 ± 0.01	1.74 ± 0.05	0.70 ± 0.02	
14378	357.875627	-54.892067	20.71 ± 0.02	1.66 ± 0.05	0.56 ± 0.02	
14844	357.899766	-54.880469	20.72 ± 0.04	1.75 ± 0.31	0.72 ± 0.09	
17455	357.997121	-54.822676	20.72 ± 0.04	1.54 ± 0.40	0.88 ± 0.12	
17729	357.875358	-54.816995	20.74 ± 0.01	1.78 ± 0.06	0.64 ± 0.02	
15068	358.094352	-54.876409	20.75 ± 0.02	1.64 ± 0.07	0.68 ± 0.02	
15994	357.763211	-54.855887	20.82 ± 0.02	1.80 ± 0.06	0.64 ± 0.02	
12892	358.014272	-54.926461	20.86 ± 0.02	1.65 ± 0.07	0.68 ± 0.02	
15697	357.897819	-54.862968	20.86 ± 0.02	1.73 ± 0.06	0.55 ± 0.02	0.3789 ± 0.0003
12589	357.785585	-54.933352	20.87 ± 0.03	1.66 ± 0.10	0.63 ± 0.03	
11976	357.893073	-54.951394	20.88 ± 0.02	1.62 ± 0.06	0.61 ± 0.02	
14664	357.901167	-54.885034	20.89 ± 0.02	1.84 ± 0.08	0.68 ± 0.02	
13901	357.824131	-54.902094	20.90 ± 0.02	1.69 ± 0.06	0.64 ± 0.02	
14595	357.914211	-54.886290	20.93 ± 0.03	1.80 ± 0.13	0.66 ± 0.03	
12863	357.874307	-54.926847	20.95 ± 0.02	1.66 ± 0.07	0.62 ± 0.02	
15156	357.891357	-54.874854	20.95 ± 0.03	1.59 ± 0.09	0.56 ± 0.03	
14825	357.922988	-54.880749	20.95 ± 0.02	1.63 ± 0.07	0.64 ± 0.02	
12650	357.958048	-54.931820	20.96 ± 0.02	1.77 ± 0.08	0.64 ± 0.02	
14407	357.917097	-54.891402	20.97 ± 0.02	1.75 ± 0.07	0.63 ± 0.02	0.3799 ± 0.0004
14939	357.872276	-54.878410	20.97 ± 0.02	1.75 ± 0.07	0.62 ± 0.02	
14944	357.913836	-54.877816	20.98 ± 0.03	2.17 ± 0.23	0.64 ± 0.05	
Other Spectroscopic Cluster Members[e]						
14271	357.899268	-54.896523	19.13 ± 0.01	1.90 ± 0.02	0.71 ± 0.01	0.3814 ± 0.0002
15403	357.908847	-54.870362	19.52 ± 0.01	1.58 ± 0.02	0.67 ± 0.01	0.3860 ± 0.0003
15827	357.957606	-54.860595	19.64 ± 0.01	1.11 ± 0.02	0.45 ± 0.01	0.3900 ± 0.0004
15400	357.866255	-54.870713	19.69 ± 0.01	1.62 ± 0.03	0.65 ± 0.01	0.3768 ± 0.0003

Table 3—Continued

Object ID[a]	RA[b]	Dec[b]	i(MAG_AUTO)[a]	$g - r$[a]	$r - i$[a]	redshift z[c]
14466	357.909595	-54.890780	20.47 ± 0.02	1.57 ± 0.05	0.60 ± 0.02	0.3827 ± 0.0002
14492	357.914762	-54.888447	20.88 ± 0.02	1.58 ± 0.06	0.64 ± 0.02	0.3899 ± 0.0004
13372	357.917399	-54.914403	20.98 ± 0.02	1.60 ± 0.06	0.65 ± 0.02	0.3803 ± 0.0003
14505	357.870029	-54.888283	21.27 ± 0.02	1.63 ± 0.08	0.66 ± 0.03	0.3860 ± 0.0003

[a]Object ID numbers are from the SExtractor catalog obtained using the i-band image for object detection. The objects are ordered from bright to faint by i-band MAG_AUTO, starting with the BCG. $g - r$ and $r - i$ colors are computed from $3''$-diameter aperture magnitudes. The errors are simply statistical errors reported by SExtractor. Not included are photometric calibration errors estimated to be 0.03-0.05 mag per filter.

[b]RA and Dec are epoch J2000.0 and are given in degrees.

[c]Redshifts measured from GMOS spectroscopy (§3.3).

[d]Galaxies, with $i < 21$, determined to be cluster members using maxBCG color selection criteria. Members are also limited to be within a radius $r_{200}^{gal} = 1.51\ h^{-1}$ Mpc ($= 6.88'$) of the BCG. See §3.2 for details.

[e]Additional galaxies determined to be cluster members via GMOS spectroscopic redshifts (§3.3), but which did not meet the maxBCG color selection criteria.

Table 4. Other Galaxies[a]

Object ID[b]	RA[c]	Dec[c]	i(MAG_AUTO)[b]	$g-r$[b]	$r-i$[b]	redshift z[d]
14193	357.895093	-54.901998	17.99 ± 0.00	1.59 ± 0.01	0.58 ± 0.00	0.2970 ± 0.0003
15313	357.893518	-54.875789	18.75 ± 0.00	1.11 ± 0.01	0.47 ± 0.01	0.2486 ± 0.0002
16682	357.903652	-54.840904	19.97 ± 0.01	1.40 ± 0.03	0.57 ± 0.01	0.3259 ± 0.0002
13520	357.887606	-54.911328	20.10 ± 0.01	0.51 ± 0.01	0.27 ± 0.01	0.0649 ± 0.0001
19352	357.902529	-54.852090	20.18 ± 0.01	1.01 ± 0.02	0.25 ± 0.01	0.4214 ± 0.0003
15509	357.941448	-54.869154	20.29 ± 0.01	1.57 ± 0.05	0.62 ± 0.02	0.4178 ± 0.0005
16409	357.890133	-54.846245	20.30 ± 0.01	0.89 ± 0.02	0.31 ± 0.01	0.3251 ± 0.0002
16570	357.911876	-54.843091	20.42 ± 0.01	0.77 ± 0.03	0.58 ± 0.02	0.1277 ± 0.0002
13423	357.960803	-54.913826	20.63 ± 0.02	1.01 ± 0.03	0.68 ± 0.02	0.2524 ± 0.0002
13620	357.889293	-54.909472	20.86 ± 0.02	1.66 ± 0.08	0.90 ± 0.02	0.5354 ± 0.0004
19257	357.902437	-54.851578	21.45 ± 0.03	0.98 ± 0.03	-0.06 ± 0.02	0.2970 ± 0.0004
16562	357.948746	-54.841891	21.58 ± 0.03	1.90 ± 0.12	0.61 ± 0.03	0.3595 ± 0.0002

[a]Galaxies determined to be non-cluster members based on GMOS spectroscopic redshifts (§3.3).

[b]Object ID numbers are from the SExtractor catalog obtained using the i-band image for object detection. The objects are ordered from bright to faint by i-band MAG_AUTO. $g-r$ and $r-i$ colors are computed from $3''$-diameter aperture magnitudes. The errors are simply statistical errors reported by SExtractor. Not included are photometric calibration errors estimated to be 0.03-0.05 mag per filter.

[c]RA and Dec are epoch J2000.0 and are given in degrees.

[d]Redshifts measured from GMOS spectroscopy (§3.3).

Table 5. NFW Fit Results

Filter	N^{a}	m_1[b]	m_2[b]	$(Q_{xx}+Q_{yy})_{min}$[c]	z_{crit}[d]	$M_{200}(10^{14}M_\odot)$[e]	c_{200}[e]	χ^2/dof[f]	P[f]
tangential shear									
g	1883	22.5	24.0	18.75	0.68	$0.1^{+0.4}_{-0.1}$	>45	0.83	0.68
r	7013	22.0	24.0	12.0	0.70	$3.9^{+2.9}_{-2.1}$	$6.5^{+5.3}_{-3.0}$	1.54	0.059
i	3296	22.0	23.5	12.0	0.71	$5.9^{+5.3}_{-3.8}$	$3.7^{+13.1}_{-2.6}$	1.55	0.055
z	2300	20.5	22.5	12.0	0.62	$11.0^{+11.9}_{-7.1}$	$1.8^{+3.6}_{-1.8}$	0.89	0.60
i+r	7995				0.70	$4.2^{+2.8}_{-2.1}$	$6.1^{+4.9}_{-3.0}$	1.58	0.048
i+r+z	8996				0.70	$5.0^{+2.9}_{-2.3}$	$4.9^{+3.9}_{-2.2}$	1.48	0.077
i+r+z+g	9424				0.70	$4.3^{+2.8}_{-2.2}$	$5.2^{+5.4}_{-2.5}$	1.50	0.069
i+r+z+SL(s)[g]	8996				0.70	$4.8^{+2.8}_{-2.2}$	$6.2^{+3.2}_{-1.7}$	1.48	0.077
i+r+z+SL(sg)[g]	8996				0.70	$4.9^{+2.9}_{-2.2}$	$5.5^{+2.7}_{-1.6}$	1.48	0.077
WL+SL+σ_c+N_{200}[h]	8996				0.70	$5.1^{+1.3}_{-1.3}$	$5.4^{+1.4}_{-1.1}$	1.48	0.077
B-mode shear									
g	1883	22.5	24.0	18.75	0.68	$1.6^{+3.1}_{-1.5}$	$6.5^{+10.1}_{-5.4}$	1.04	0.41
r	7013	22.0	24.0	12.0	0.70	$0.1^{+0.1}_{-0.1}$	>63	1.19	0.25
i	3296	22.0	23.5	12.0	0.71	$0.1^{+0.4}_{-0.1}$	>0	0.91	0.58
z	2300	20.5	22.5	12.0	0.62	$5.5^{+10.7}_{-5.2}$	$0.3^{+1.2}_{-0.3}$	0.61	0.91
i+r	7995				0.70	$0.1^{+0.1}_{-0.1}$	>51	1.10	0.34
i+r+z	8996				0.70	$0.1^{+0.1}_{-0.1}$	>27	0.80	0.71
i+r+z+g	9424				0.70	$0.1^{+0.6}_{-0.1}$	>0	0.77	0.75

[a]Number of galaxies used in the weak lensing analysis in each filter. For the multi-filter samples N is the number of *unique* galaxies.

[b]SExtractor `MAG_AUTO` magnitude limits used to define the galaxy sample.

[c]Minimum Ellipto size $Q_{xx}+Q_{yy}$ used to define the galaxy sample.

[d]The source redshift at which $1/\Sigma_{crit}$ is the same as the effective value computed by integration over the source galaxy redshift distribution, as described in §5.3.

[e]Best-fit NFW profile parameters: mass M_{200} and concentration c_{200}. Errors are 1-parameter, 1σ values, as determined by where $\Delta\chi^2 = 1$. The uncertainties on M_{200} are rounded off to the nearest $0.1 \times 10^{14} M_\odot$. Note that for most of the cases (primarily B-mode fits) where there is no significant mass detection, we provide only a 1σ lower limit on c_{200}, which is otherwise not constrained on the high side even at 1σ, up to the upper bound value $c_{200} = 10^4$ that we have checked. Joint 2-parameter error contours for select samples are shown in Fig. 13.

[f]χ^2 per degree of freedom (dof) relative to a null hypothesis of zero shear. (This is *not* the χ^2/dof of the NFW fit, which is very close to one in all cases.) P is the probability of exceeding the observed χ^2/dof. The number of degrees of freedom for this χ^2 test is always 20, i.e., the number of radial bins plotted in Figures 10-12.

[g]Fit results derived from combined weak plus strong lensing ("SL") constraints. "(s)" denotes the case where we estimated the dark matter mass within the Einstein radius by subtracting off just a stellar mass contribution, while "(sg)" is the case where we also subtracted off an estimated gas mass contribution. See §6.1 for details.

[h]Fit results derived from combined weak lensing ($i + r + z$), strong lensing (SL(sg)), cluster velocity dispersion (σ_c), and cluster richness (N_{200}) constraints. See §6.2 for details.

Table 6. Source Galaxy Star Formation Rates[a]

Knot	$f(\nu)_{[OII]}$ (erg s^{-1} cm^{-2})	$f(\nu)_L$ (erg s^{-1} cm^{-2})	$f(\nu)_S$ (erg s^{-1} cm^{-2}Hz^{-1})	SFR (($f_{lens} = 39$) $M_\odot$ yr^{-1})	SFR (($f_{lens} = 141$) $M_\odot$ yr^{-1})
A1	$1.06 \pm 0.04 \times 10^{-15}$	$1.71 \pm 0.06 \times 10^{-16}$	$1.36 \pm 0.02 \times 10^{-28}$	3.9 ± 1.1	1.1 ± 0.4
A2	$0.84 \pm 0.04 \times 10^{-15}$	$1.43 \pm 0.06 \times 10^{-16}$	$1.43 \pm 0.02 \times 10^{-28}$	3.1 ± 0.9	0.85 ± 0.4
A3	$2.09 \pm 0.10 \times 10^{-15}$	$1.28 \pm 0.06 \times 10^{-16}$	$0.51 \pm 0.01 \times 10^{-28}$	7.7 ± 2.2	2.1 ± 0.4
A4	$1.02 \pm 0.02 \times 10^{-15}$	$2.83 \pm 0.06 \times 10^{-16}$	$2.33 \pm 0.02 \times 10^{-28}$	3.7 ± 1.1	1.0 ± 0.4

[a]See §7 for the definitions of the various fluxes $f(\nu)$. Fluxes quoted are measured values. f_{lens} is the lens magnification.